CREEP OF OLIVINE DURING HOT-PRESSING

by

Mary Bernadette Schwenn

B.S., University of Utah
1972
M.S., San Diego State University
1974

SUBMITTED IN PARTIAL FULFILLMENT
OF THE REQUIREMENTS FOR THE
DEGREE OF MASTER OF
SCIENCE

at the

MASSACHUSETTS INSTITUTE OF
TECHNOLOGY

September, 1976
(i.e. February, 1977)

Signature of Author...
Department of Earth and Planetary Sciences
September, 1976

Certified by...
Thesis Supervisor

Accepted by...
Chairman, Departmental Committee on Graduate Students

ABSTRACT

THE CREEP OF OLIVINE DURING HOT-PRESSING

by

Mary Bernadette Schwenn

Submitted to the Department of Earth and Planetary Sciences on September 30, 1976 in partial fulfillment of the requirements for the degree of Master of Science.

Olivine powders of grain sizes ranging from 1 to 2000 μm were hot-pressed at temperatures between 1000°C and 1650°C and at differential stresses between 100 and 400 bars.

In our hot-pressed specimens, all grains, both coarse and fine, deformed plastically. In addition, the coarse grains fractured; the fine grains did not. The coarse-grained specimens contained a large proportion of fines; the densification of the coarse-grained powders was aided by the densification of these fine-grain-sized particles.

An average stress exponent, n, of 1.5±0.4 was obtained from differential tests on the fine-grained aggregates ($G<25$ μm); while an average n of 3.4±0.8 was found for the medium-grain-sized aggregates tested (25-250 μm). The activation energy obtained for all the hot-presses powders was 85±29 kcal/mole. In addition, the strain rate for the fine-grained aggregates varied approximately as the third power of the grain size. However, the grain size dependence of the strain rate for medium- to coarse-grained aggregates was masked by the presence of fines in these aggregates.

There was an indication in our hot-pressing data that the effect of oxygen fugacity on strain rate was unimportant. However, hydrogen fugacity appeared to 'soften' olivine.

Uncertainities in the formulation of hot-pressing models limits the accuracy with which hot-pressing data can be used to predict uniaxial creep behavior of the corresponding dense aggregate. Creep data predicted in this way results in an expansion of the Coble field in the Stocker and Ashby (1973) map and a corresponding contraction in the power-law creep field as compared with the previous estimates.

Thesis Supervisor: C. Goetze
Asst. Professor of Geology

ABSTRACT

THE CREEP OF OLIVINE DURING HOT-PRESSING

by

Mary Bernadette Schwenn

Submitted to the Department of Earth and Planetary Sciences on September 30, 1976 in partial fulfillment of the requirements for the degree of Master of Science.

Olivine powders of grain sizes ranging from 1 to 2000 m were hot-pressed at temperatures between 1000°C and 1650°C and at differential stresses between 100 and 400 bars.

In our hot-pressed specimens, all grains, both coarse and fine, deformed plastically. In addition, the coarse grains fractured; the fine grains did not. The coarse-grained specimens contained a large proportion of fines; the densification of the coarse-grained powders was aided by the densification of these fine-grain-sized particles.

An average stress exponent, n, of 1.5 ± 0.4 was obtained from differential tests on the fine-grained aggregates ($G < 25 \mu m$); while an average n of 3.4 ± 0.8 was found for the medium-grain-sized aggregates tested (25-250 μm). The activation energy obtained for all the hot-pressed powders was 85 ± 29 kcal/mole. In addition, the strain rate for the fine-grained aggregates varied approximately as the third power of the grain size. However, the grain size dependence of the strain rate for medium- to coarse-grained aggregates was masked by the presence of fines in these aggregates.

There was an indication in our hot-pressing data that the effect of oxygen fugacity on strain rate was unimportant. However, hydrogen fugacity appeared to 'soften' olivine.

Uncertainties in the formulation of hot-pressing models limits the accuracy with which hot-pressing data can be used to predict uniaxial creep behavior of the corresponding dense aggregate. Creep data predicted in this way results in an expansion of the Coble field in the Stocker and Ashby (1973) map and a corresponding contraction in the power-law creep field as compared with the previous estimates.

Thesis Supervisor: C. Goetze
Asst. Professor of Geology

ACKNOWLEDGEMENTS

I wish to thank C. Goetze for his help in preparing this work. I would also like to thank S. Parker for the unhesitating way in which she gave her time and effort to help me type this thesis.

TABLE OF CONTENTS

Chapter

LIST OF FIGURES

CHAPTER II

CHAPTER III

CHAPTER IV

LIST OF TABLES

CHAPTER I

INTRODUCTION

1.1 Introduction

Hot-pressing of refractory materials is a commonly used fabrication process (c.f. Ceramic Fabrication Processes, Kingery (ed.), 1958). It is of interest to geophysics and rock mechanics from an experimental standpoint since artificial "rocks" of controlled grain size and purity can be prepared for the further testing of physical properties, such as creep behavior (Nicholas et al., 1975; Paterson and Weaver, 1970; Crouch, 1972; Warshaw and Norton, 1962; Passmore et al., 1966), electrical conductivity (Duba, 1972; Dvorak, 1973; Bradley et al., 1964), and ultrasonic velocities (Anderson and Kanamori, 1968; Ahrens et al., 1969). We report here quantitative data relating the density, grain size, time, temperature, and compacting stress for olivine powders both to assist others in designing the fabrication of aggregates of suitable quality as well as to shed light on the creep properties of very-fine-grain-sized olivine, a subject on which there is very little data at present (Twiss, 1976).

1.2 Hot-Pressing

Sintering is essentially a process in which an aggregate of fine particles, in contact with each other, consolidates when heated to a suitable temperature. Hot-pressing is a pressure-sintering technique, i.e., an external pressure is applied to a powder at a suitable temperature to increase the rate of consolidation as the powder sinters. In hot-pressing, the driving force for densification is due to both the surface energy and the applied pressure. Hence this technique results in a decrease in both the porosity and surface area, and, consequently, in a simultaneous increase in the bulk density without the extensive grain growth and recrystallization that frequently occur if the specimen were sintered to the same final density. Since the time and temperature needed for densification is reduced, materials can be hot-pressed to higher final densities than those that would be obtained from sintering.

CHAPTER II

EXPERIMENTAL TECHNIQUES

2.1 The Experiments

In this study, olivine powders of grain sizes ranging from 1μm to 2000μm were hot-pressed at temperatures between 980°C and 1600°C and at differential stresses between 100 and 400 bars. All tests performed on these olivine powders were isothermal, constant-load tests. However, in a number of experiments, either the differential stress was cycled between two levels at a constant temperature to determine the stress exponent, or the temperature was cycled at a constant stress to determine the activation energy, Q.

2.2 Sample Preparation

The starting material. Powders were prepared from crystals of San Carlos peridot of composition Fo_{92}. From optical micrographs of the starting material, it was determined that these powders were composed of regular, equiaxed but anhedral grains. The degree of roundness of the individual grains varies with the grain size range -- the coarser grain size fractions containing a larger proportion of irregular, angular grains than the finer grain size fractions. An optical micrograph of the starting material for one size fraction is shown in Figure 2-1.

Durham (1975) determined that the starting material has a free dislocation density of between 10^4 and $10^5 cm^{-2}$ and a total dislocation density, including subgrain walls, of between 10^5

Figure 2-1

Optical micrograph of the starting material. The specimens were prepared by hand-grinding and ball-milling crystals of San Carlos peridot (Fo_{92}) and were separated using standardized sieves. A 25-53μm grain size fraction is shown in the micrograph.

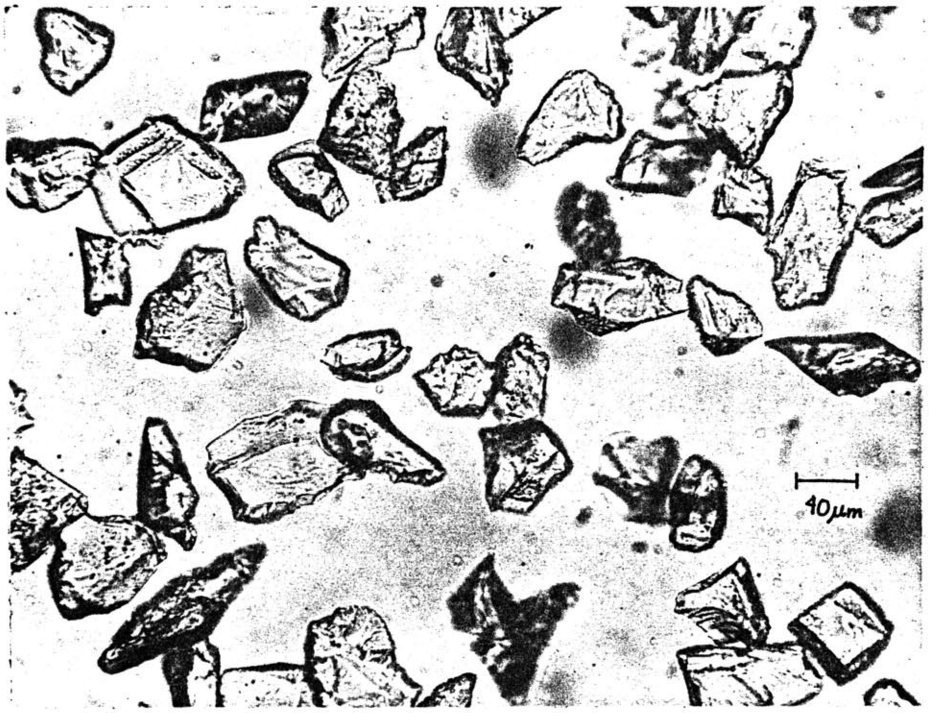

FIGURE 2-1

and $10^6 cm^{-2}$. Using infrared spectroscopy, Caristan (1976) determined that the H/Si ratio in the starting material is less than 28 ppm. Consequently, the starting material can be classified as "dry" olivine.

Powder preparation. Powders of varying size fractions were obtained from the starting material by hand-grinding and ball-milling. Bits of iron from the ball were removed from the resulting powders using a magnet. The grain size fractions used in the experiments were separated using standardized sieves. The finest size fractions, i.e., those less than 25μm, were separated by a modified pipette analysis.

2.3 The Apparatus

Pressure-sintering was performed in the one-atmosphere deformation apparatus described by Kohlstedt and Goetze (1974) and shown in Figure 2-2. All runs, except S13 (c.f. Table 3-1), were deformed with a servo-controlled constant-load apparatus in which the load is applied to the die assembly by compressing a spring of known spring constant using a servo-controlled piston. A direct current differential transformer (DCDT) measured the shortening of the spring, and this output is fed back to the servo-controller to maintain a constant spring displacement. This apparatus uses a gas-tight seal around the sliding steel plug; and it was found that the O-ring around the plug will support up to 0.8 kg at room temperature. The maximum uncertainty in the applied load, σ_a, arising from frictional losses in the

Figure 2-2

Apparatus used for high-temperature low-stress deformation in a flowing gas atmosphere.

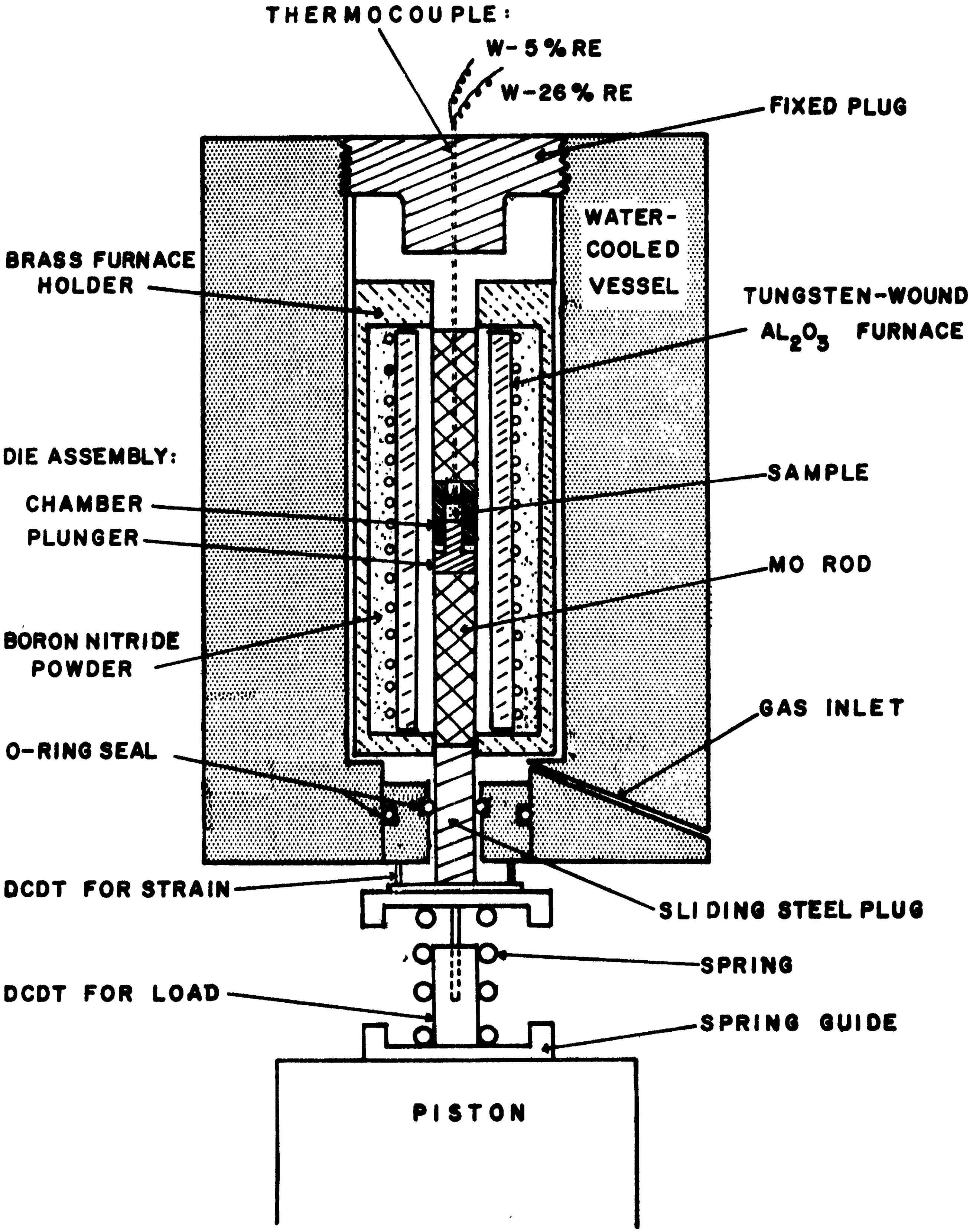
THERMOCOUPLE:
W-5% RE
W-26% RE
FIXED PLUG
WATER-COOLED VESSEL
BRASS FURNACE HOLDER
TUNGSTEN-WOUND AL_2O_3 FURNACE
DIE ASSEMBLY:
CHAMBER
PLUNGER
SAMPLE
MO ROD
BORON NITRIDE POWDER
GAS INLET
O-RING SEAL
DCDT FOR STRAIN
SLIDING STEEL PLUG
SPRING
DCDT FOR LOAD
SPRING GUIDE
PISTON

FIGURE 2-2

O-ring seal has been estimated to be 3% at σ_a = 100 bars, 1.5% at σ_a = 200 bars, etc., based on the 0.8 kg load for a 0.25" diameter plunger. Run number S13 was deformed using an apparatus similar to that described above except that a dead-weight-loading configuration (Durham, 1975) was employed. Since this configuration does not use a gas-tight seal around the steel plug, the frictional losses in the applied load are negligible.

The load is supported in the furnace by molybdenum rods 1/2" in diameter. Deformation of this column under stress occurs as the sample reaches its final density and the rods deform as rapidly as the specimen. Measurement of the lengths of each rod before and after a run allowed the deformation of the column to be subtracted from the recorded piston displacement. The effect of the column deformation is negligible for σ_a = 800 bars; it amounts to about 0.2% strain if a molybdenum plunger is used in the die assembly and about 0.03% strain at 166 bars if a tungsten plunger is used.

The die assembly (Figure 2-2) consists of a cylindrical chamber composed of molybdenum, 0.25" in interior diameter and 0.50" in exterior diameter; and a 0.25" diameter sliding plunger, composed of molybdenum in runs S1-S12 and tungsten in all later runs, by which stress is applied to the specimen. In run S13, the interior diameter of the chamber and the diameter of the plunger were reduced to 1/16" diameter to decrease the sample size, but this sample size reduction increased the uncertainties in specimen height. The chamber bore is flat-bottomed to reduce uncertainty in the specimen height; from optical measurements of the bottom curvature, the uncertainty in the specimen height was determined to be less than 1%. Since the plunger strained slightly (less than 0.4% for molybdenum and 0.13% for tungsten as 166 bars) during each experiment, a 0.005" diameter difference between the plunger and the chamber was used to prevent the piston from seizing up. The maximum uncertainty in specimen height resulting from the squeezing of powder into the space between the chamber and the plunger walls has been extimated to be less than ±0.5%.

To reduce pressure variations arising from uneven filling of the die and from wall friction, the length-to-diameter ratio of the specimens was minimized. The initial length-to-diameter ratios of all specimens vary from 0.4 to 0.7. The pressure distribution in compacting a powder in a cylindrical die, pressing from one end, is shown in Figure 2-3 (from Kingery, 1960). Examination of optical micrographs prepared from vertical sections through several specimens, however, showed no apparent variation in either the final density or the grain size throughout the specimen.

The specimen was heated using a tungsten-wound Al_2O_3 furnace that maintained a ½" hot-zone. The sample and the thermocouple were positioned within this hot-zone. At 1200^oC, the temperature within the hot-zone varied by less than 1^oC; so we estimated the temperature gradient along the specimen to be less than 5^oC at $T = 1600^oC$. Temperature was measured by positioning a W-5% Re/W-25% Re thermocouple inside the molybdenum

Figure 2-3

Pressure distribution in compacting a powder in a cylindrical die, pressing from one end. Lines of constant pressure are shown. Maximum resistance to compactness comes from wall friction, and the pressure variation increases as the length-diameter ratio of the die cavity is increased (After Kingery, 1960).

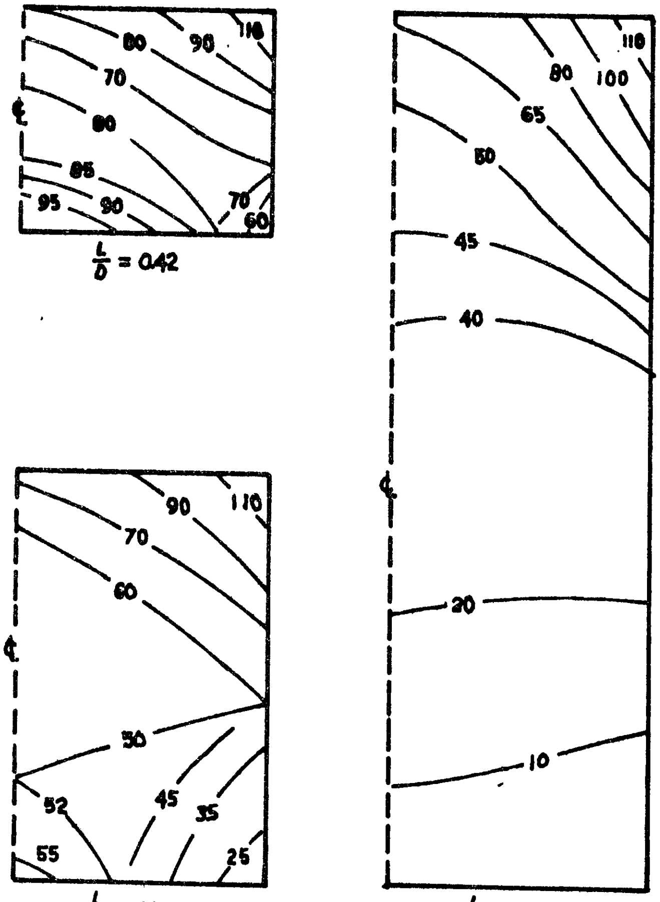

$\frac{L}{D} = 0.42$

$\frac{L}{D} = 0.79$

$\frac{L}{D} = 1.66$

FIGURE 2-3

column at the base of the die assembly, 1/8" from the base of the specimen; so the absolute temperature at the specimen should be known within ±10°C at T = 1600°C. Hence the uncertainty in strain rate at constant stress is less than ±12% using Q = 85 kcal/mole. Temperature is held constant to within about ±4°C throughout a run by connecting the output of the thermocouple directly to a temperature controller.

The sample is maintained within the stability field of Fo_{92} at high temperature (Muan and Osborne, 1965, p. 50 and p. 26; Nitzan, 1974) by controlling oxygen fugacity. In all experiments except S-19 and S-20, fugacity was controlled by flowing a 70% H_2/30% CO_2 (by volume) gas mixture through the furnace at the room temperature rate of 1 cm^3/sec; while in experiments S-19 and S-20, the oxygen fugacity was controlled by flowing a CO_2/CO gas mixture ($\text{Log } P_{CO_2}/P_{CO} = -1.39$ for S-19 and 0.38 for S-20). These gas mixtures maintain the sample near the reducing side of the olivine stability field.

Densification of the specimen was obtained from the summed output of a pair of DCDTs mounted on each side of a sliding steel plug. The output from these DCDTs was fed to an X-Y strip chart recorder that plotted the movement of the plug as a function of time. The density of a sample at any given time during densification was given by $\rho_b = (M/A)h^{-1}$, where ρ_b is the bulk density of the sample; M, its mass; A, its cross-sectional area; and h, its height. Since M and A were constant for the hot-pressing die, the sample density was directly related to its height. For each run, the values of M and A were determined initially and the final specimen was measured directly with a micrometer, where possible, or its length obtained from the final length of the die assembly. Also, where possible, the final density of each specimen was determined using the Archimedes liquid displacement technique, with carbon tetrachloride as the suspending liquid. Using these values, the percent porosity, $\% \phi$, at any given time during the run could be determined from the relation:

$$\%\phi = 100\left(1 - \frac{\rho_b}{\rho_{th}}\right) \qquad (2\text{-}1),$$

where ρ_{th} is the theoretical density of the specimen; the instantaneous strain rate, $\dot{\varepsilon}$, of the sample during any given time interval from the relation given in Equation 4-4. We estimated that the uncertainty in the porosity is less than ±1% and in the strain rate, less than ±5%.

2.4 Experimental Procedure

The weight of the sample was determined initially, and the initial lengths of the plunger, unloaded die assembly, and column parts, measured. The sample was then loaded into the die, and the die, cold-pressed with an arbor-press to insure that the die was evenly filled. The initial length was then determined from the difference in lengths between the loaded and unloaded die assemblies.

The loaded die was inserted into the deformation apparatus described in Section 2.3, and a small load (10-20 bars at the sample) applied to insure physical contact of the column parts. As the displacement and temperature were recorded on the strip chart as functions of time, the temperature was raised to a predetermined level. When the desired temperature was reached, the load was applied. A rapid 5° -10°C cooling of the sample resulted during the initial application of the load as the column parts made better contact. After this initial cooling, however, the temperature of the column remained constant.

To eliminate any complications in analysis arising from the variation in pore radii at any particular density (Section 4.1), we used a relatively high applied stress so that the driving force of the surface energy (Appendix A) would be small compared to that of the applied stress. Consider a 5-10 μm sample at 0.1% porosity. Its median grain size was determined optically to be 7.2 μm; its median pore radii, 0.4 μm; We estimate the driving force due to surface energy in this case to be about 19 bars, or 11% of σ_a = 166 bars, and 6.5% of σ_a = 291 bars. See Section A-2.

At the end of the run, the final lengths of the plunger, loaded die assembly, and column parts were measured with a micrometer. From the difference in lengths of the final loaded die assembly and the unloaded die assembly, the final specimen height could be obtained. Where possible, the sample was removed intact, and both its final length and final density, measured. In these cases, the uncertainty in sample height arising from the bore curvature and the squeezing of powder between the chamber and plunger walls could be eliminated. These latter measurements were then used to interpret the strip chart record. The change in the lengths of the column parts was calculated, and the change in length with time, subtracted from the displacement record to correct for any straining of the column parts or plunger.

To summarize, we believe the uncertainties in stress to be within ±10%; and in strain rate, within ±5%, although for some specimens it may be larger below 5% porosity.

CHAPTER III

RESULTS

3.1 The Hot-Pressed Specimens

Where possible, optical micrographs were prepared for dense specimens. What porosity remained in these specimens was almost exclusively concentrated at the grain boundaries as is evident in Figures 3-1a and 3-1b. There was no apparent variation in either the grain size or density throughout these specimens, and no evidence of discontinuous grain growth in any of them. In decorated micrographs (Kohlstedt et al., 1976) prepared from the medium- and fine-grain-sized specimens, dislocations were observed to be uniformly distributed throughout the individual grains. See Figure 3-1c. All, even the coarser grain sizes, showed variable extinction typical of plastically deforming olivine (Kirby and Raleigh, 1973); but variable extinction was not observed in the starting material. Evidently every grain in our hot-pressed specimens was stressed and was deforming plastically in response to the applied stress.

The fine-grained specimens (less than about 53μm) were observed to contain only fine-grain sizes with polygonal, equiaxed shapes, as is evident in Figures 3-1a and 3-1b. For example, examination of the micrograph prepared for one 5-10μm specimen (S14) showed that the median grain size of the polygonal, equiaxed grains was 7μm (determined from the mean intercept length defined by Underwood, pp. 42-43, 1973), and that less than 10% of the specimen contained grain sizes greater than 10μm. Similar

Figures 3-1a and 3-1b

Optical micrographs of dense hot-pressed specimens. The remaining porosity in these specimens is concentrated almost entirely at the grain boundaries. No apparent variation in density or grain size are evident in either micrograph. Also these is no evidence of discontinuous grain growth in either.

(a) Sample S-1: A 25 μm and less (bimodal) starting size fraction deformed at 166 bars and 1000°C and 1234°C in a CO_2/H_2 atmosphere. $\%\phi_f$ is4.2%. The porosity appears to consist mainly of isolated, spherical pores.

(b) Sample S-14: A 5-10 μm specimen deformed at temperatures between 1019°C and 1324°C and stresses between 110 and 350 bars. $\%\phi_f$ is 0.1%, as determined by immersion.

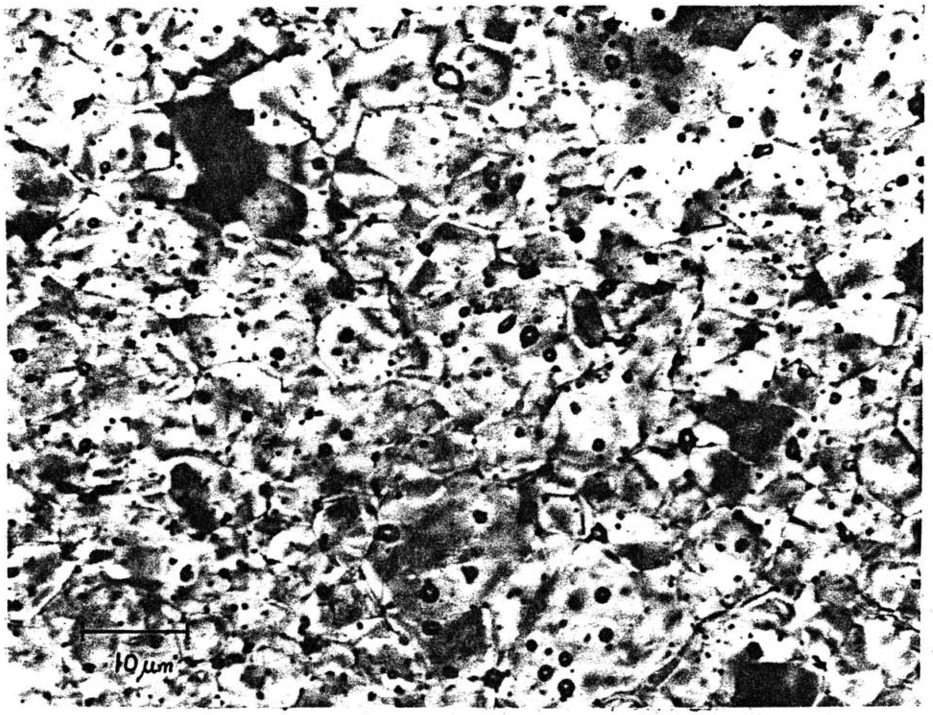

FIGURE 3-1a

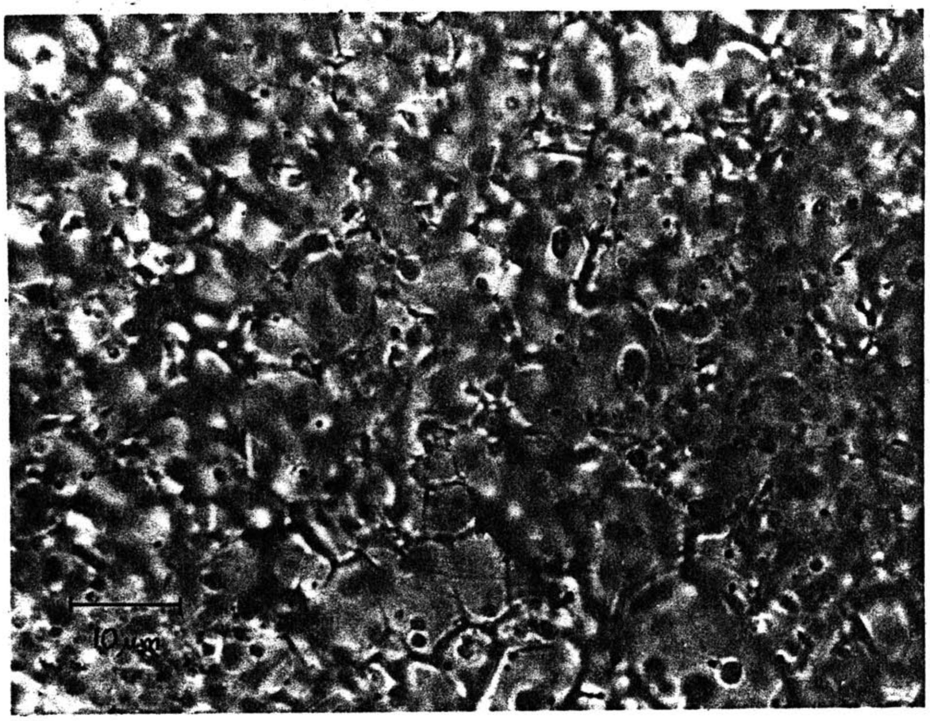

FIGURE 3-1b

observations were made on two of the 25 µm and less specimens (S-1 and S-2). Specimen S-2 contained a uniform distribution of polygonal particles with the median grain size, 22 µm. Less than 6% of this specimen was composed of particle sizes greater than 25 µm. Specimen S-1, though, contained a bimodal distribution of grain sizes -- approximately 50% in the 4-5 µm size range and 50% in the 20-25 µm range. Finally, in one 25-53 µm specimen run in a CO_2/H_2 atmosphere (S-4), about 18% of the specimen was composed of grain sizes between 9 and 20 µm (average grain size = 12 µm) with the remainder of the specimen in the 25-53 µm size fraction (average size = 27 µm). The presence of finer-grain sizes in this hot-pressed piece (S-4) was probably the result of clumping of the starting material during sieving.

The coarse-grained specimens, on the other hand, were observed to contain large fractions of equiaxed, fine-grain sizes concentrated between the coarser-grained particles which more or less retained the shapes of the starting material. This is evident in the micrograph in Figure 3-2. We believe that the fines in these coarser-grained specimens were probably formed by particle fragmentation during arbor-pressing of the specimen and at the onset of loading, and that densification of the coarser-grained specimens is aided by the densification of the fine-grain-sized particles in these specimens. For example, both the 105-250 µm specimens (S-3 and S-8) contained at least 20% fines in the 40-90 µm range, as compared with a 90-195 µm grain size range (average size = 112 µm) in the remainder of the specimen. Similarly, the 500-1000 µm specimen (S-12) contained fines mostly in

Figure 3-1c

Optical micrograph of dislocations in one grain of specimen S-8 -- a 105-250 μm powder hot-pressed at 166 bars and 1590°C. The specimen was decorated at 900°C for about 1 hour. The dislocations in this specimen appear to be uniformly distributed throughout the grains.

Figure 3-2

Optical micrograph of a hot-pressed specimen, S-12. The starting size fraction for the specimen shown was 500-1000 μm. This powder was tested at 166 bars and 1600°C. The coarse-grained particles in this micrograph are mostly between 450 and 900 μm; while the fines are between 40 and 195 μm. We believe that densification of such a coarse-grained specimen is aided by the densification of the fine-grained particles.

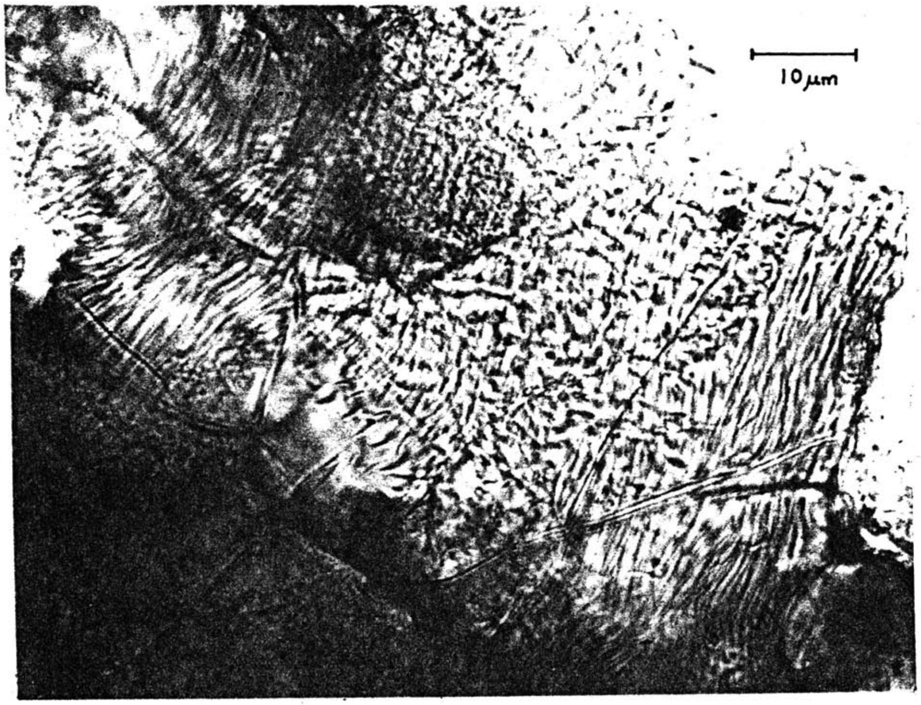

FIGURE 3-1c

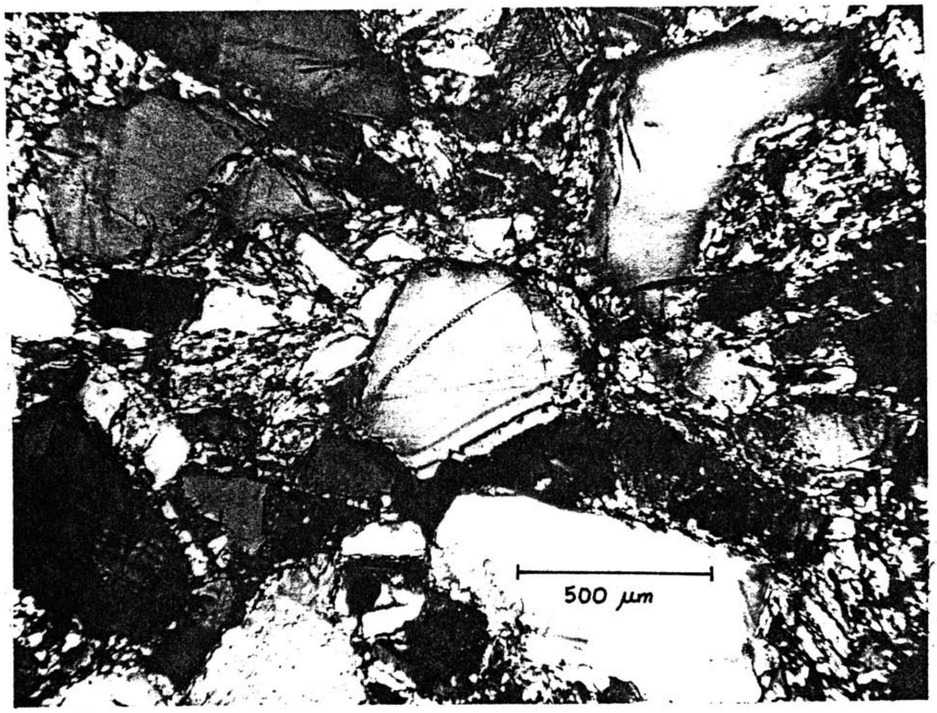

FIGURE 3-2

the 40-195 μm range (average about 80 μm) and angular, irregular, coarse-grained particles mostly in the 450-1000 μm range.

3.2 Densification Curves

The experimental data are tabulated in Appendix B; and the experimental conditions under which each experiment was run, in Table 3-1. The stress, temperature, and grain size of each specimen are given in Table 3-1, and both the $\text{Log}_{10}\ \dot{\varepsilon}$ at 15% porosity and the $\text{Log}_{10}\ \dot{\varepsilon}$ at 15% porosity, corrected to an arbitrarily-chosen common temperature of 1429°C, are included for each test.

Densification curves for each constant-stress test are shown in Figure 3-3 which records the relative density, D = actual density/single crystal density of 3.373 gm/cm^3, as a function of total elapsed time for each test. From the figure, it is evident that D increases with time. For a particular grain size and temperature, an increase in the applied stress (S-3) increases the densification rate for that test. A similar increase in the densification rate is observed when the temperature is increased during a constant-load test. Finally, it is observed that the finer-grained specimens reach a particular value of D at lower temperatures than the coarser-grained specimens.

Plotting D versus elapsed time averages the length changes, and consequently, the strain rate over time. Therefore, to obtain values for the stress exponent, n, and the activation energy, Q, it is necessary to plot the instantaneous strain rate as a function of the porosity, ϕ = 1-D, as in Figures 3-4a and 3-4b. Considerable variation in the initial porosity of the

TABLE 3-1

EXPERIMENTAL DATA FOR HOT-PRESSED OLIVINE

Run #	Grain Size (μm)	Stress (bars)	Temperature (°C)	$-\text{Log}\ \dot{\varepsilon}$ at %ϕ=15%	$-\text{Log}\ \dot{\varepsilon}_{1429}$ at %ϕ=15%
S-1	25 and less (bimodal)	166	1000	6.77	3.09
			1234	3.93	2.52
S-2	20-25	166	1565	3.142	3.95
S-3	105-250	166	1469	4.37	4.62
		298		3.61	3.86
		200		4.30	4.55
S-4	25-53	166	1465	4.06	4.29
S-5	1000-2000	166	1430	6.13	6.14
S-7	250-500	166	∿1433	5.75	5.78
S-9	1000-2000	166	1587	5.35	6.28
S-11	250-500	166	∿1594	4.95	5.91
S-12	500-1000	166	1600	5.23	6.23
S-13	5-10	149	1284	3.07	2.05
S-14	5-10	110	1019	--	--
		177	1019	--	--
		350	1019	--	--
		110	1120	∿6.72	∿4.30
		210	1120	∿6.48	∿4.06
		110	1232	4.81	3.38
		177	1232	4.61	3.18
		110	1334	3.64	2.99
		177	1334	3.42	2.77
		210	1334	--	--
S-15	1000-2000	291	1624	3.64	4.76

TABLE 3-1 (Cont'd.)

Run #	Grain Size (μm)	Stress (bars)	Temperature (°C)	-Log $\dot{\varepsilon}$ at %ϕ=15%	-Log $\dot{\varepsilon}_{1429}$ at %ϕ=15%
S-16	20-25	291	1008	--	--
		110	1157	--	--
		291	1176	5.19	3.28
		110	1244	5.27	3.94
		110	1305	5.14	4.28
		176	1305	4.81	3.95
		291	1305	4.41	3.55
S-17	10-15	176	1173	4.67	2.74
		209		4.64	2.71
		243		4.61	2.68
		273		4.63	2.70
		291		4.58	2.65
S-18	15-20	169	1047	5.63	2.47
			1112	5.12	2.62
			1159	4.88	2.82
		292	1159	4.55	2.49
S-19	25-53 (CO_2/CO)	170	1393	5.52	5.28
			1549	4.10	4.82
S-20	25-53 (CO_2/CO)	170	1413	5.38	5.28
		246	1413	4.84	4.74
		246	1545	3.83	4.53

<u>Figure 3-3</u>

Plot of relative density, D, versus the elapsed time, where D = (actual density/single crystal density). The curves represent actual data for all hot-pressing runs except the differential tests. The experimental conditions under which each test was conducted can be obtained by referring to Table 3-1.

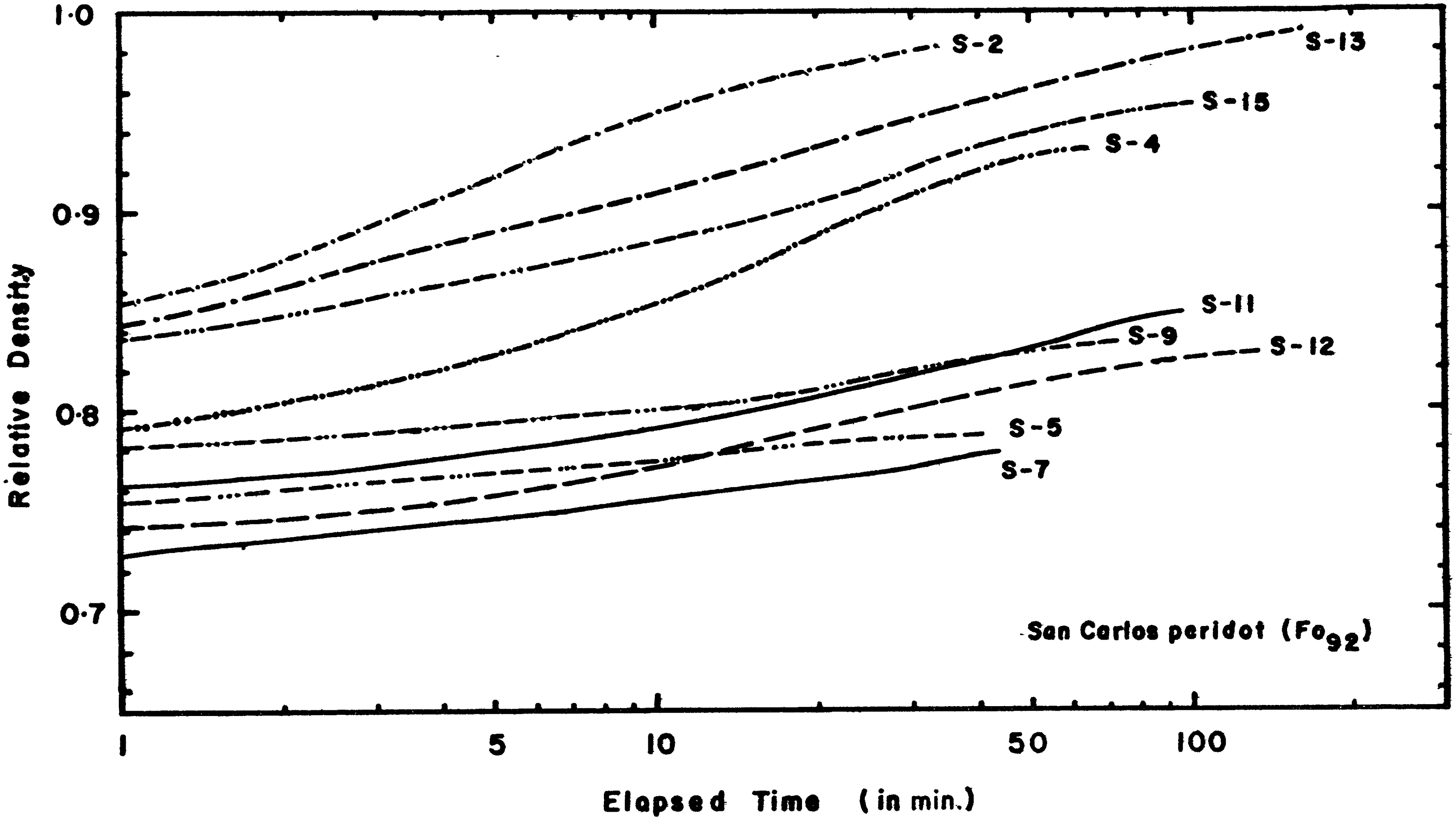
1·0
0·9
0·8
0·7
Relative Density
1
5
10
50
100
Elapsed Time (in min.)
S-2
S-13
S-15
S-4
S-11
S-9
S-12
S-5
S-7
San Carlos peridot (Fo_{92})

FIGURE 3-3

Figure 3-4

Log_{10} of the instantaneous strain rate is plotted versus porosity for 3 25-53μm hot-pressing tests. It is apparent that all three curves have the same general shape, except at the beginning and end; so the general variation of $\text{Log}_{10}\ \dot{\varepsilon}$ with can be described by a single curve.

(a) Run #S-4: 1465°C; 166 bars; CO_2/H_2 atmosphere (30% CO_2; 70% H_2 by volume).

(b) Run #S-19: 1393°C and 1549°C; 170 bars; CO_2/CO atmosphere with log $P_{CO_2}/P_{CO} = -1.39$.
Run #S-20: 1413°C and 1545°C; 170 and 246 bars; CO_2/CO atmosphere with log $P_{CO_2}/P_{CO} = 0.38$.

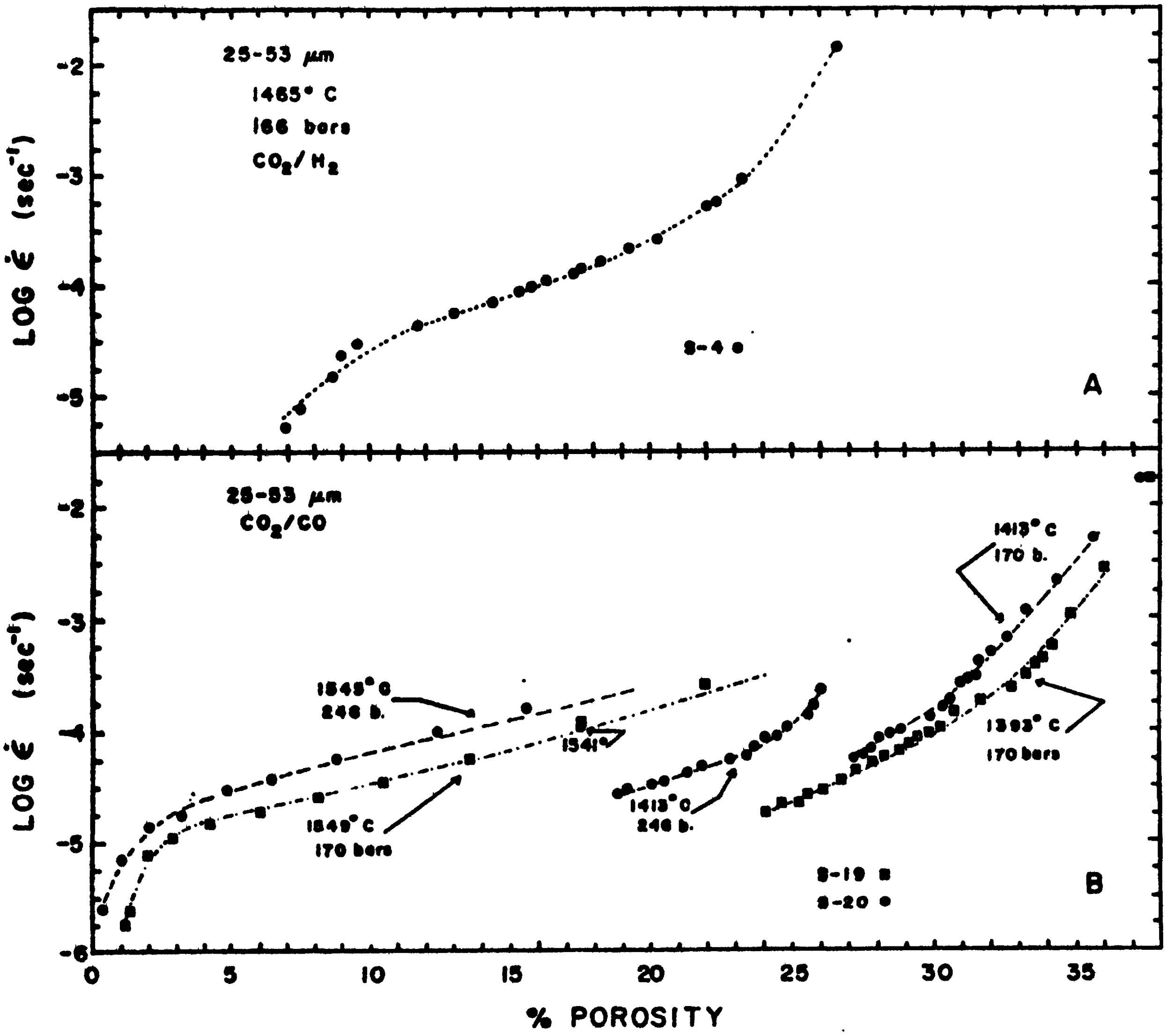
25-53 μm
1465° C
166 bars
CO₂/H₂
S-4 ●
A
25-53 μm
CO₂/CO
1413° C
170 b.
1545° C
246 b.
1541°
1549° C
170 bars
1413° C
246 b.
1393° C
170 bars
S-19 ■
S-20 ●
B
LOG ε̇ (sec⁻¹)
LOG ε̇ (sec⁻¹)
-2
-3
-4
-5
-2
-3
-4
-5
-6
0
5
10
15
20
25
30
35
% POROSITY

FIGURE 3-4

specimens is evident in these figures since the degree of packing in a particular specimen depends upon both the grain size and the compaction of the specimen by the arbor-press. Also a large change in the strain rate without significant densification occurs at the onset of the load as a result of particle fragmentation and rearrangement. This initial rapid densification rate is not evident in Figure 3-3 as it is completed within the first minute. The final density reached by any specimen is determined by the grain size, temperature, and stress conditions of the test; as a final density is approached for any given test conditions, the densification rate, and consequently, the Log $\dot{\varepsilon}$ decrease. Some runs were terminated by the seizure of the plunger in the die, as is evident from the sharp change in the slope of the Log $\dot{\varepsilon}$ curves over the last few percent of attained porosity (Figure 3-4A) and for run S-4 shown in Figure 3-3.

We will assume that the general variation in Log $\dot{\varepsilon}$ values with porosity can be described by a single curve, the slope of which has been determined from the trend of the data in Figure 3-4. This general curve shape has been fitted to all tests; and the Log $\dot{\varepsilon}$ values both at 15% porosity and at the temperature and stress jumps have been determined from this best-fit curve. For all tests, the largest deviations of the experimental data from the general curve occur immediately after the initial onset of the load and during the last 5% of attained porosity. The typical agreement of these curves with the data is shown in Figure 3-4.

3.3 The Effect of Temperature on the Strain Rate

The effect of temperature on the strain rate for each grain size was studied by cycling the temperature between predetermined values during a constant-load test (differential tests). Since densification during pressure-sintering is often described by an equation of the form:

$$\dot{\varepsilon} = A\,\sigma^n \exp(-Q/RT) \qquad (3\text{-}1),$$

where $\dot{\varepsilon}$ is the strain rate: A, a constant; σ, the applied stress; Q, the activation energy for the deformation process involved in densification; n, the stress exponent related to the specific deformation mechanism; R, the gas constant; and T, the temperature (Coble, 1970; Wilkinson and Ashby, 1975; Urick and Notis, 1973), the values of the activation energy, Q, at a constant stress and grain size could then be determined using the relationship:

$$Q = -R\,\frac{(\ln \dot{\varepsilon}_1 - \ln \dot{\varepsilon}_2)}{(\frac{1}{T_1} - \frac{1}{T_2})} \qquad (3\text{-}2).$$

The values of Q determined in this manner are summarized in Table 3-2 and plotted versus porosity in Figure 3-5. Additional data were obtained by plotting the Log $\dot{\varepsilon}$ at 15% porosity and constant stress as a function of $\frac{1}{T}$ for each grain size. This plot yields the temperature dependence of the creep rate during the hot-pressing of olivine. This second set of data is plotted in Figure 3-6. From the slope of the curves in Figure 3-6, the activation energies for each grain size can be determined. There appears to

Figure 3-5

Activation energies, Q, determined from differential tests are plotted against the porosity at which the jump in temperature occurred. Symbols (▽, ⊙, etc.) on plot refer to the grain size of the specimen. There appears to be no systematic variation of Q with either the porosity, stress, or grain size, so far as tested.

Symbols:

▽ 5-10μm
▲ 10-15μm
✡ 15-20μm
◎ 20-25μm
⊙ 25μm and less
+ 25-53μm (CO_2/H_2)
⊕ 25-53μm (CO_2/CO)
◈ 105-250μm
△ 250-500μm
⊡ 1000-2000μm

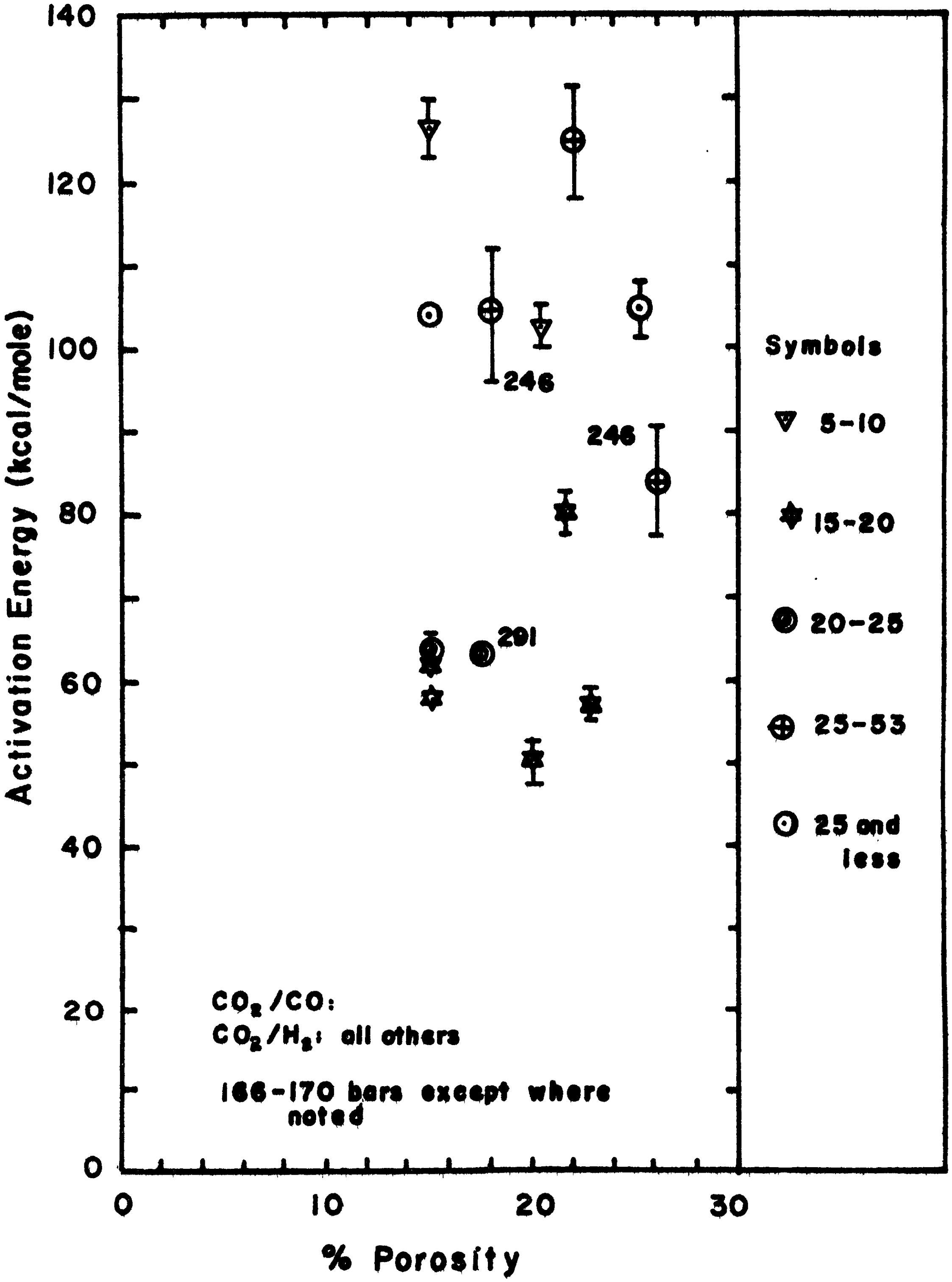
Activation Energy (kcal/mole)
140
120
100
80
60
40
20
0
% Porosity
0
10
20
30
246
246
291
Symbols
▽ 5-10
✡ 15-20
◎ 20-25
⊕ 25-53
⊙ 25 and less
CO_2/CO:
CO_2/H_2: all others
166-170 bars except where noted

FIGURE 3-5

TABLE 3-2

N AND Q DETERMINED FROM DIFFERENTIAL TEST DATA

Run #	Grain Size (μm)	Stress (bars)	Temperature (°C)	Porosity	n	Q(kcal/mole)
S-1	25 & less (bimodal)	166	1000 1234	25.2	--	104.7
S-3	105-250	166 298	1469	19.4	3.11	--
		298 200		18.5	3.61	
		200 298		12.0	3.66	--
S-14	5-10	110 177	1019	37.3	3.73	--
		177 350	1019	36.6	4.99	--
		177	1019 1234	32.2	--	113.0
		110	1120 1232	30.0	--	153.3
		110 177	1232			
		110	1232 1333	20.5	--	102.6
		110 177	1333	4.0	1.21	--
		177	1232 1333	4.0	--	139.9
S-16	20-25	110 176	1305	23.3	2.28	--
		176 291	1305	21.6	2.15	--
		291	1305 1176	17.4	--	63.3
		110 291	1305	16.5	1.68	--

TABLE 3-2 (Cont'd.)

Run #	Grain Size (μm)	Stress (bars)	Temperature (°C)	Porosity	n	Q(kcal/mole)
S-17	10-15	176 209	1173	21.2	1.48	--
		209 243	1173	19.0	1.38	--
		243 273	1173	16.4	1.49	--
		273 291	1173	15.2	1.80	--
S-18	15-20	169	1047 1112	21.6	--	79.8
		169 292	1159	21.6	1.14	--
		169	1047 1112 1159	20.0	--	50.2 50.2
		169 292	1159	20.0	1.18	--
		169 292	1159	22.8	1.13	--
			1047 1112 1159	22.8		46.3 56.9
S-19	25-53 (CO_2/CO)	170	1393 1549	22.0	--	124.9
S-20	25-53 (CO_2/CO)	170 246	1413	26.0	3.49	--
		246	1413 1545	26.0	--	83.8
		246	1413 1545	18.0	--	104.7

Figure 3-6

$\mathrm{Log}_{10}\ \dot{\varepsilon}$ as a function of 1/T ($°C^{-1}$) for various grain size hot-pressed specimens tested at 166 bars. All values of $\mathrm{Log}_{10}\ \dot{\varepsilon}$ plotted were picked from the experimental curves at a porosity of 15%. All Log $\dot{\varepsilon}$ values, except where noted, are for tests conducted at 166 bars. From the slope of the curves in this figure, the activation energy can be computed. A curve with the slope Q = 85 kcal/mole has been included for comparison. The symbols used in this figure are the same as those in Figure 3-5.

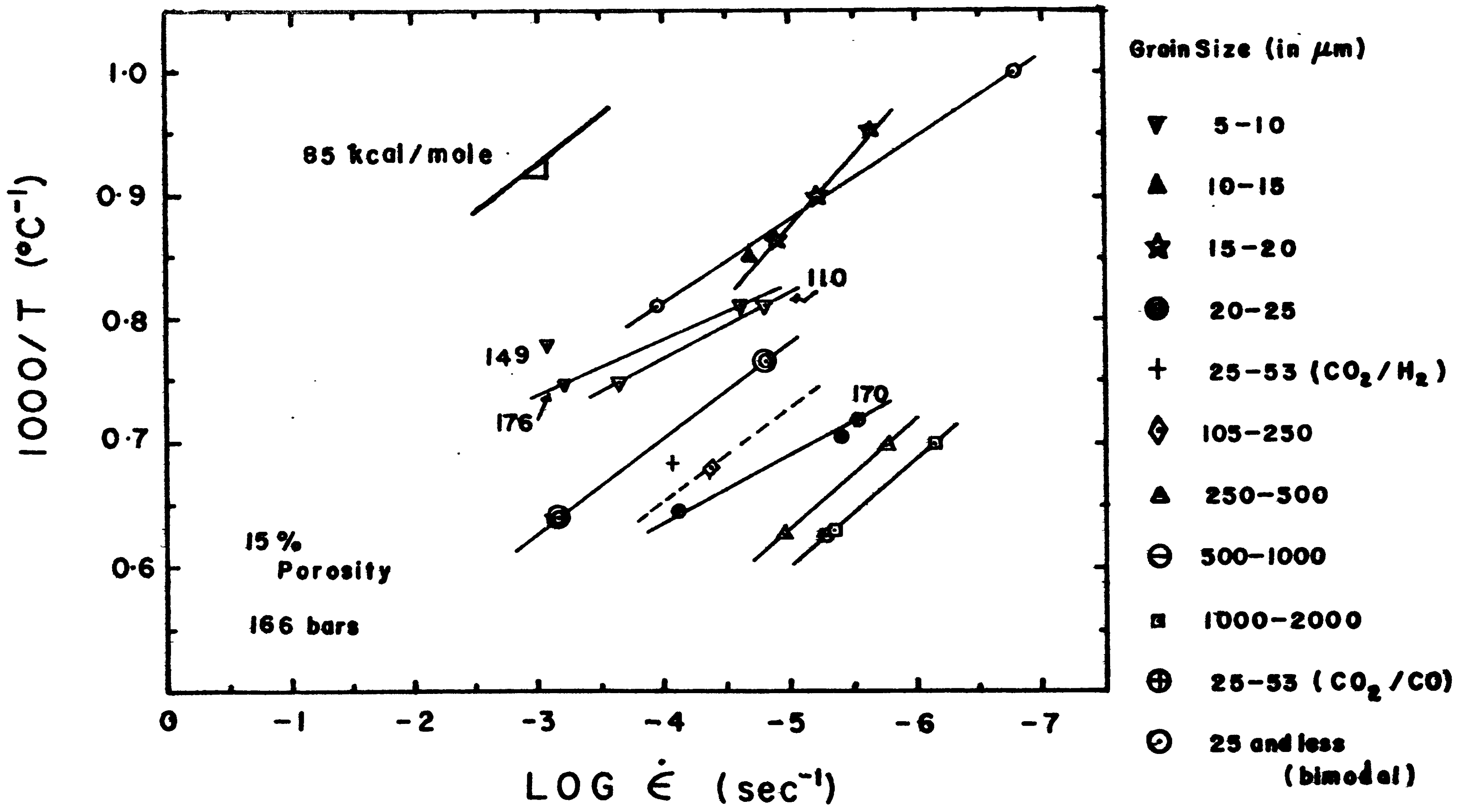
1.0
0.9
0.8
0.7
0.6
1000/T (°C⁻¹)
0
-1
-2
-3
-4
-5
-6
-7
LOG Ė (sec⁻¹)
85 kcal/mole
110
149
176
170
15 %
Porosity
166 bars
Grain Size (in μm)
▼ 5-10
▲ 10-15
★ 15-20
● 20-25
+ 25-53 (CO₂/H₂)
◊ 105-250
△ 250-500
⊖ 500-1000
⊡ 1000-2000
⊕ 25-53 (CO₂/CO)
⊙ 25 and less (bimodal)

FIGURE 3-6

be no systematic variation of the activation energy with either stress, grain size, or porosity so far as tested. The median value of Q determined from both the differential test data for porosities between 10% and 25% (Figure 3-5) and from the curves in Figure 3-6 is 85±29 kcal/mole.

3.4 The Effect of Stress on the Strain Rate

The effect of stress on the strain rate was determined by cycling the specimens at constant temperature between predetermined values of the applied stress. Again the formulation of Coble (1973) and Wilkinson and Ashley (1976) given in Equation 3-1 was used but this time for a constant temperature; and the value of the stress exponent, n, could then be determined at a particular porosity from the strain rates, $\dot{\varepsilon}_1$ and $\dot{\varepsilon}_2$, for each stress, σ_1 and σ_2, respectively, from the expression:

$$n = \frac{\ln \dot{\varepsilon}_1 - \ln \dot{\varepsilon}_2}{\ln \sigma_1 - \ln \sigma_2} \qquad (3\text{-}3).$$

The variation of n with porosity and grain size is plotted in Figure 3-7. The values of n determined at each porosity and grain size from the stress jumps are tabulated in Table 3-2. For a given grain size, inaccurate values of n are determined at the beginning and end of the run since the densification rate is changing rapidly for a given change in the porosity. From Figure 3-7, it was observed that the average value of n is about 3.4 ±0.8 for the medium-grain-sized specimens, 25-53μm and 105-250μm, but only 1.5 ±0.4 for fine-grained specimens, of grain sizes less than 25μm.

Figure 3-7

The stress exponents, n, determined from all differential tests are plotted against the porosity at which the jump in stress occurred. The symbols in the figure refer to the grain size of the specimen and are the same as those in Figures 3-5 and 3-6. For the range of porosity, 10-25%, there is no systematic variation of n with porosity. The variation of n with grain size is evident -- the fine-grained specimens having an average n of 1.5 ± 0.4; while the medium-grain-sized specimen, average n of 3.4 ±0.8.

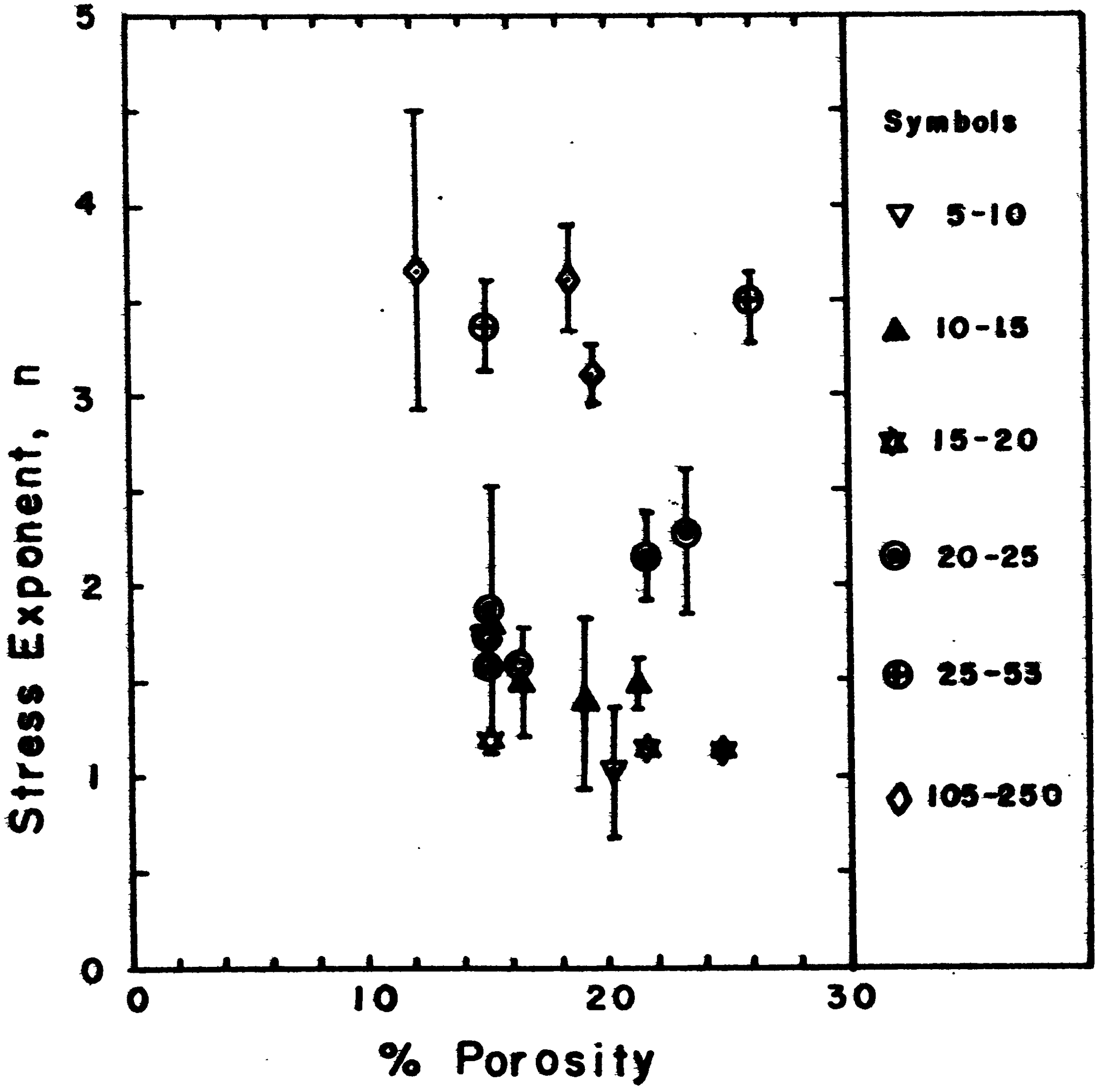
Stress Exponent, n
% Porosity
0
1
2
3
4
5
0
10
20
30
Symbols
▽ 5-10
▲ 10-15
✡ 15-20
◎ 20-25
⊕ 25-53
◇ 105-250

FIGURE 3-7

3.5 The Effect of Grain Size on the Strain Rate

To determine the effect of grain size on strain rate, it is necessary to reduce all data to a common temperature; we have arbitrarily chosen 1429° C. The $\mathrm{Log}_{10}\ \dot{\varepsilon}$ values for each grain size were determined at 15% porosity and 1429° C from the curves in Figure 3-6. Only the curves for tests conducted at stresses between 166 and 170 bars were used. For those grain sizes where the slope of the curve in Figure 3-6 was not known, the $\mathrm{Log}_{10}\dot{\varepsilon}$ values were calculated assuming an activation energy of 85 kcal/mole. The strain rates so determined are plotted as a function of grain size in Figure 3-8. The slope of the curve which 'best-fits' the data in this figure shows the strain rate to be inversely proportional to approximately the third power of the grain size for grain sizes below about 53 μm, and indicates that the grain size dependence decreases as the grain size is increased above 53 μm.

3.6 The Effect of Atmosphere and Oxygen Fugacity on Creep Rate

Three 25-53 μm specimens were hot-pressed to determine if the oxygen fugacity and the atmosphere have any effect on the creep rate. In order to compare these tests, corrections are needed for temperature and stress. The $\mathrm{Log}\ \dot{\varepsilon}$ values for all 25-53 μm specimens at 15% porosity were normalized to a common temperature of 1429°C using Figure 3-6 and an activation energy equal to 85 kcal/mole. The fugacity values obtained at different temperatures were also normalized to a common temperature of 1429°C using the stability field determined by Nitsan (1974) for

Figure 3-8

$\mathrm{Log}_{10}\ \dot{\varepsilon}$ values are shown for each grain size at 15% porosity and a common temperature of 1429°C. Only Log $\dot{\varepsilon}$ values obtained from tests conducted at stresses between 166 and 170 bars were used. The grain size fraction at each value of Log $\dot{\varepsilon}$ are plotted are plotted as vertical bars; the uncertainities in Log $\dot{\varepsilon}$, as horizontal bars. The 'best-fit' curve through the data suggests that the $\dot{\varepsilon}$ for fine-grained powders ($G<25\mu m$) varies as the inverse third power of the grain size.

Also included in the figure are Log $\dot{\varepsilon}$ versus grain size curves obtained from the rate equations for Coble and power-law creep, c.f. Equations 4-2 and 4-3, respectively. Each curve assumes a different formulation for the effective stress, σ_{eff}. See Section 4-1. The grain size at which the transition from Coble to power-law creep occurs has been determined for each model, and this transition is shown for each σ_{eff} model as a horizontal line in the heavily stipled region.

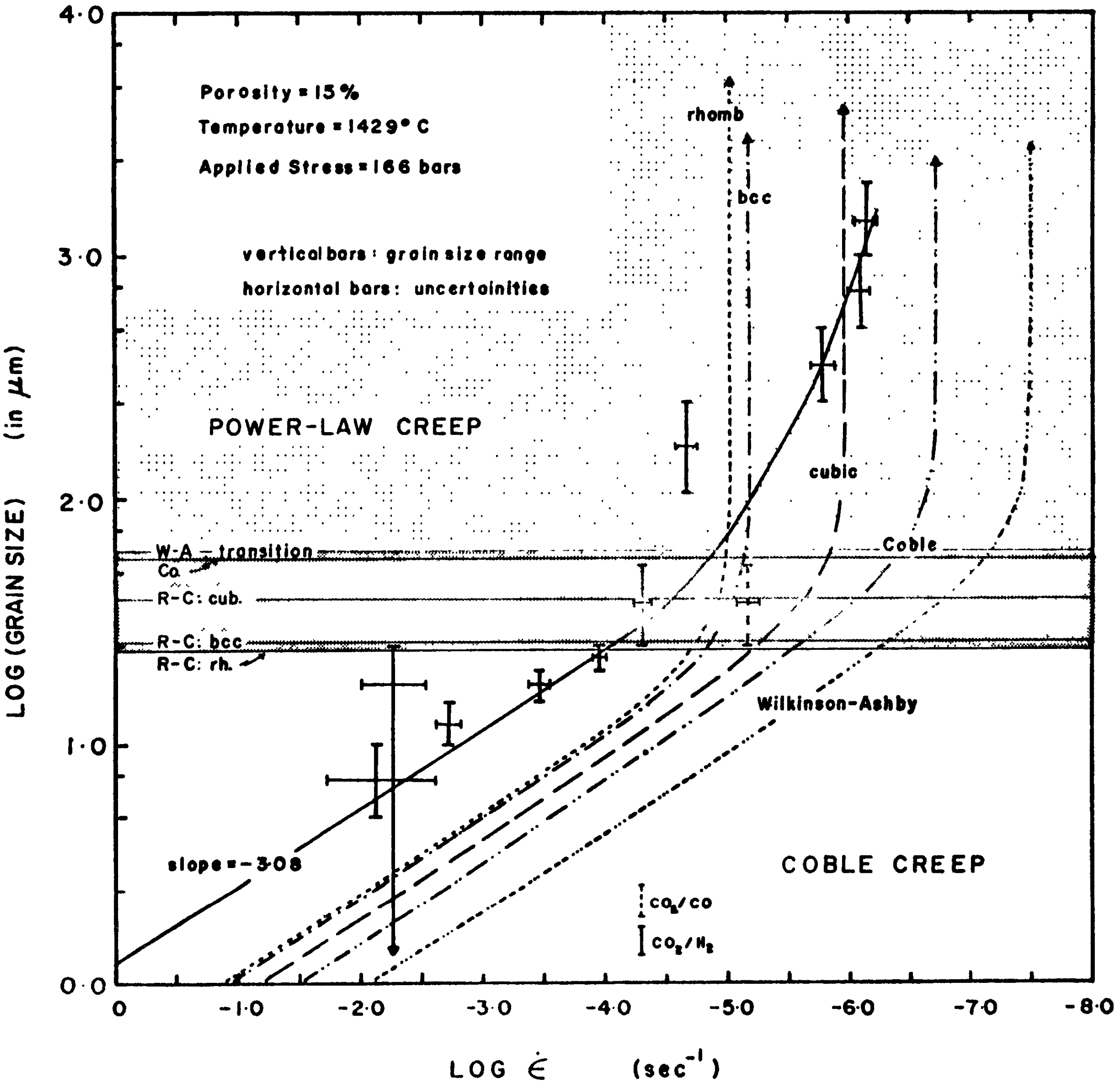

Porosity = 15%
Temperature = 1429° C
Applied Stress = 166 bars
vertical bars: grain size range
horizontal bars: uncertainities
POWER-LAW CREEP
COBLE CREEP
rhomb
bcc
cubic
Coble
Wilkinson-Ashby
W-A - transition
Co.
R-C: cub.
R-C: bcc
R-C: rh.
slope = -3.08
CO2/CO
CO2/H2
LOG (GRAIN SIZE) (in μm)
LOG ε̇ (sec-1)
4.0
3.0
2.0
1.0
0.0
0
-1.0
-2.0
-3.0
-4.0
-5.0
-6.0
-7.0
-8.0

Figure 3-8

Fo_{92} as a function of oxygen fugacity and temperature. That is, the experimentally determined oxygen fugacities were normalized by $f_1=10^{-10.49}$, the oxygen fugacity of Fo_{92} at the reducing end of the stability field for a temperature of 1429°C. See the insert in Figure 3-9. The resulting values of Log $\dot{\varepsilon}$ as a function of oxygen fugacity are plotted in Figure 3-9 for a common stress of 166 bars, assuming $n=3$, a common temperature of 1429°C, and 15% porosity. The strain rate determined for the 25-53 μm specimen from the curve that "best-fits" the data in Figure 3-8 has also been plotted in Figure 3-9 as a solid dot. We observe that there is little variation of strain rate with oxygen fugacity for the specimens hot-pressed in a CO_2/CO atmosphere. Kohlstedt and Goetze (1974) also noted that the effect of oxygen fugacity on strain rate was small. Also, there is an indication that the strain rate for the samples deformed in the CO_2/H_2 atmosphere is faster by a factor of 3 to 5 than the strain rate of those specimens deformed in a CO_2/CO atmosphere.

Figure 3-9

Log $\dot{\varepsilon}$ values at 15% porosity are plotted versus the oxygen fugacity for three 25-53 μm specimens. All Log $\dot{\varepsilon}$ values were normalized to a common temperature of 1429°C using the curves in Figure 3-6 or an activation energy of 85 kcal/mole. All Log $\dot{\varepsilon}$ values were also normalized to a common stress of 166 bars, assuming the stress exponent, n, equaled 3. In addition, the oxygen fugacity values were normalized to a common temperature of 1429°C using the fugacity for the reducing end of the stability field of Fo_{92}, i.e., $f_1 = 10^{-10.49}$. See the insert in Figure 3-9 (from Figure 1, Nitsan, 1974).

It is evident in Figure 3-9 that there is little variation of Log $\dot{\varepsilon}$ with oxygen fugacity, but there is an indication that the Log $\dot{\varepsilon}$ values obtained in a CO_2/H_2 atmosphere are faster by a factor of 3 to 5 than those values obtained in a CO_2/CO atmosphere. For comparison, the Log $\dot{\varepsilon}$ value determined from the curve that 'best-fits' the data in Figure 3-8 was plotted in Figure 3-9 as a solid dot.

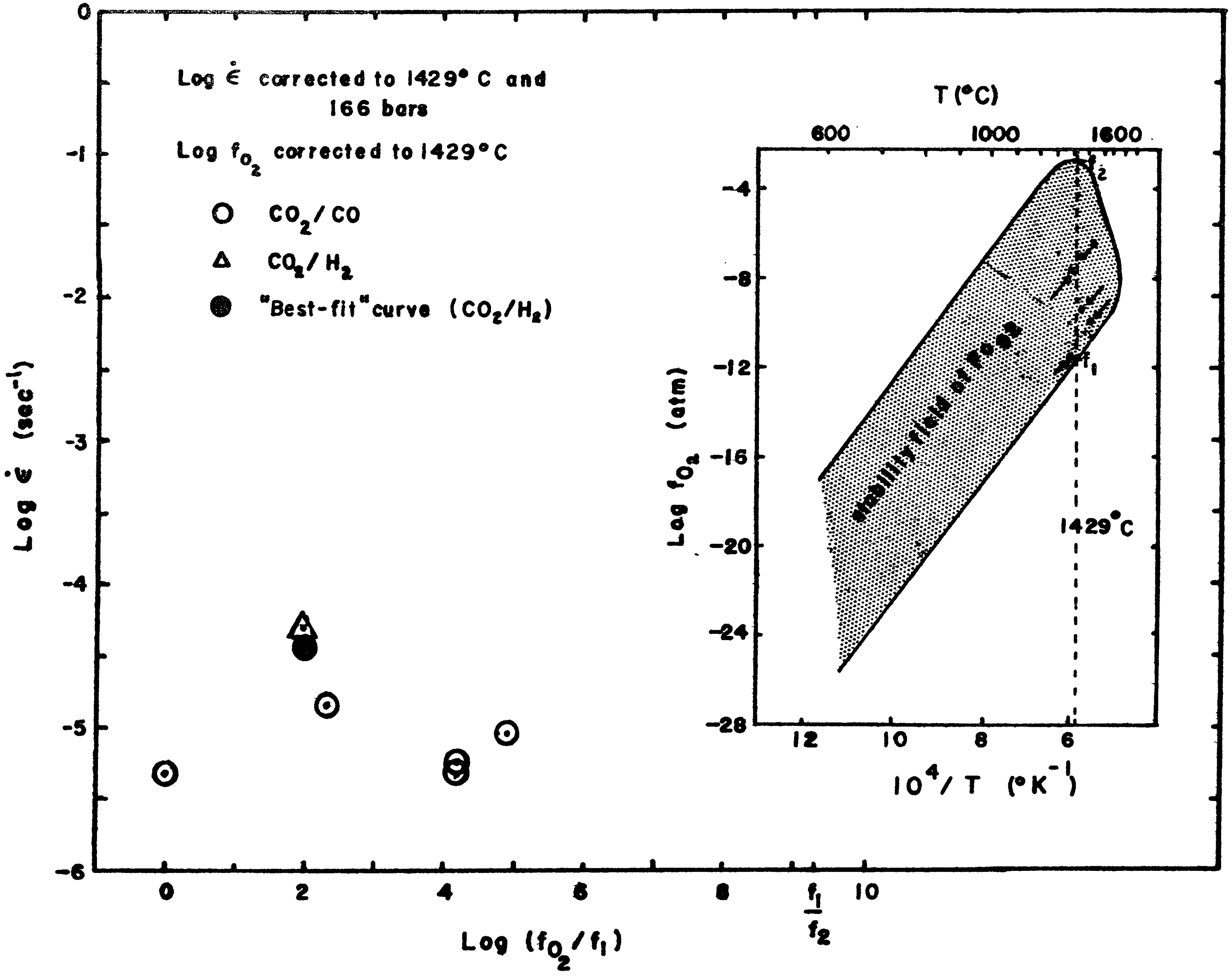
Log $\dot{\epsilon}$ corrected to 1429° C and 166 bars
Log f_{O_2} corrected to 1429°C
○ CO_2/CO
△ CO_2/H_2
● "Best-fit" curve (CO_2/H_2)
Log $\dot{\epsilon}$ (sec^{-1})
0
-1
-2
-3
-4
-5
-6
0
2
4
6
8
10
$\frac{f_1}{f_2}$
Log (f_{O_2}/f_1)
T (°C)
600
1000
1600
Log f_{O_2} (atm)
-4
-8
-12
-16
-20
-24
-28
12
10
8
6
$10^4/T$ (°K^{-1})
f_2
f_1
1429°C
stability field of Fo92

FIGURE 3-9

CHAPTER IV

DISCUSSION

4.1 Adaptation of Theories of High-Temperature Creep to Hot-Pressing

Adaptation of the high-temperature creep models for Nabarro-Herring creep (Nabarro, 1948; Herring, 1950), Coble creep (Coble, 1963), and power-law creep (Weertman, 1968; Argon, 1968) to hot-pressing appears to be straightforward and has been done by a number of authors, including Coble (1970) and Wilkinson and Ashby (1975). The rate-equations obtained for hot-pressing are formulated in terms of fundamental constants (D_B, Ω, etc.) and are for Nabarro-Herring creep (Coble, 1970):

$$\frac{\dot{D}_{NH}}{D} = \frac{40\, D_v \Omega}{3kTG^2}\ P \qquad (4\text{-}1),$$

where D is the relative density; G, the grain size in cm.; D_v, the lattice diffusion coefficient; Ω, the atomic volume; and P, the stress driving densification (discussed below); and for Coble creep (Coble, 1970):

$$\frac{\dot{D}_C}{D} = \frac{47.5\ D_b \Omega \delta}{kTG^3}\ P \qquad (4\text{-}2),$$

where δ is the grain-boundary width; and D_b, the grain boundary diffusion coefficient; and for power-law creep (Wilkinson and Ashby, 1975):

$$\frac{\dot{D}_{PLC}}{D} = \left[\frac{A_1 \mu \vec{b}}{kT\mu^n}\right] \exp(-Q_c/kT)\ P^n \qquad (4\text{-}3),$$

where A_1 is a material constant; $\vec{b}$, the Burger's vector; Q_c, the activation energy for creep; and μ, the shear modulus. These rate-equations permit the evaluation of the kinetics with density when all the fundamental constants are known. Unfortunately, these data are not available for most materials. For example, data are available for power-law creep in olivine, but not for Coble creep.

The high-temperature creep equations cannot be rigorously applied to predict the time dependence of densification (Coble, 1970) because the flow equations are assumed to terminate at the grain boundaries rather than at the pores. Because of this, the adaptation of the high-temperature creep equations to hot-pressing can only approximate the instantaneous rate of densification. In addition, the effective stress, discussed below, which motivates material transport, is not precisely known in terms of the applied pressure and the porosity.

Derivation of hot-pressing rate equations from the high-temperature creep equations. Since the mass, M, of a powder compact and its cross-sectional area, A, are constant in a hot-pressing die, the sample density, $\rho = (M/A)h^{-1}$, is directly related to the sample height, h. When this relation is differentiated with respect to time, an expression is obtained relating the linear strain rate, $\dot{\varepsilon}$, in the high-temperature creep models with the densification rate, $\dot{D}$, for hot-pressing:

$$\dot{\varepsilon} = -\frac{1}{h}\dot{h} = \frac{1}{D}\dot{D} \qquad (4\text{-}4).$$

The linear strain rate, given on the left-hand side of Equation

4-4 can be obtained directly from measurements of plunger travel in a die.

The applied stress, σ, in the high temperature deformation models is replaced by an expression:

$$P = \sigma_{eff} + \frac{2\gamma}{r} - P_i \qquad (4-5),$$

incorporating the effective stress, σ_{eff}, discussed below; the driving force due to surface energy, $2\gamma/r$ (final-stage densification); and the internal pore pressure, P_i.

Assuming the pore radius, r, can be approximated by

$$r = (1-D)^{1/3}(G/2) \qquad (4-6),$$

where G is the grain size in cm. (Coble, 1970), the driving force resulting from the surface energy (Appendix A) at 1% porosity is negligible compared with the applied stress. For example, for a 7μm powder, the surface energy term is 6% of the applied stress, σ_a = 166 bars; and for a 150μm powder, 3% of σ_a. Also, the internal pore pressure, P_i, may be neglected for the hot-pressed specimens in this study. If it is assumed that all pores close at 5% porosity (this assumption will be discussed in detail below), the internal pressure in pores of a 7μm powder will only be 8 bars at 1% porosity and 87 bars at 0.1% porosity.

Equation 4-4 relates the densification during hot-pressing, D, to the linear strain rate in the high-temperature creep models. When the linear strain rate, $\dot{\varepsilon}$, in these models is replaced by $\dot{D}$ and the applied stress, σ, by the stress driving densification, P, given in Equation 4-5, the hot-pressing rate equations given in Equations 4-1, 4-2, and 4-3 are obtained. These equations are valid for the intermediate stage, up to 95% theoretical density, of hot-pressing, i.e., when the compact has sintered to the point where the pores between grains are roughly cylindrical in shape. The expressions appropriate for the final stage of densification, when the compact contains only isolated, spherical pores, have been derived by Coble (1970) and Wilkinson and Ashby (1975) by modeling the compact by a thick, isolated spherical shell centered on a spherical pore. However, the densification rates predicted for the final stage of sintering differ only by a small numerical factor from those, for the intermediate-stage of densification.

Theory of pore closure during hot-pressing. In a porous body undergoing sintering, the pores tend to remain at the lowest energy sites, i.e., the grain boundaries. Since the grain-boundary energies are usually less than half of the material's surface energy, the dihedral angle of the pore is high and it is thus reasonable to model the pore shape by a cylinder (Budworth, 1969). This is the pore shape assumed in intermediate-stage hot-pressing. The cylindrical shape becomes unstable with respect to the surface energy of the pore when the length of the cylinder becomes equal to its circumference. At this stage during sintering (final stage), the cylindrical pores pinch off and close. The closed pores are isometric in shape (optical examination confirms this); so it is generally assumed that during the final stage of densification, the pores are spherical in shape.

The critical value of porosity, where the cylindrical pores start to pinch off and close, has been computed by Budworth (1969). Assuming that the cylindrical pores can be modeled by truncated octahedra, the critical porosity is 16%; but for a surface energy model, the critical porosity is 8%. The later model is more realistic. The values of critical porosity actually observed are between 5% and 15%.

As Budworth's calculation suggests, the pores in a powder compact remain entirely open until about 85% of theoretical density is reached. At this time, some pores begin to close; the number of pores closing increases slowly at first and then more rapidly until all pores are closed at about 95% of theoretical density.

Rao and Chaklader (1972) do not distinguish in their model whether the pores are connected or not; while Coble (1970) and Wilkinson and Ashby (1975) need to know both the appropriate pore shape and whether or not the pores are closed. Coble derives the densification equations for diffusional creep by assuming the pores remain open until 95% of theoretical density is attained. To derive an expression that is valid for the final 5% of densification, the powder compact is modeled by a thick, isolated spherical shell of material of radius, b, centered on a spherical hole of radius, a. This simply introduces a small numerical factor into the densification equation. Wilkinson and Ashby (1975), on the other hand, assume that the powder compact contains only isolated, spherical pores once 80% of theoretical density is reached. Although their model is not precise, the densification rates they obtain will only differ by a small numerical factor from those obtained by Coble (1970).

The effective stress during hot-pressing. Because of porosity, the applied stress producing a given amount of strain in a porous aggregate is greater than the stress producing an equivalent strain in a single crystal. Although the effective stress varies with both the porosity and the pore shape, it is generally assumed that the effective stress is a function of porosity alone; and that the pore shape remains constant over the densification interval to which a hot-pressing model is applied.

The effective stress motivates material transport during hot-pressing. During the initial stage of hot-pressing, the contact stress, and, consequently, the effective stress must be large because the contact area is very small. However, as deformation of the points of contact proceeds, the contact stresses and the effective stress will gradually decrease. Finally, as theoretical density is approached, the effective stress decreases to a value equal to the applied stress.

Attempts to characterize the highly variable differential stresses within individual grains of an aggregate during hot-pressing have been the subject of several papers (McClelland, 1964; Spriggs et al., 1964; Farnsworth and Coble, 1966; Rao and Chaklader, 1973; Wilkinson and Ashby, 1975). In order to adopt the rate-equation for hot-pressing (Murray et al., 1958):

$$\frac{dD}{dt} = \frac{P}{3\eta}(1-D) \qquad (4\text{-}7)$$

to flow in crystalline materials, McClelland (1964) introduced an expression for the effective stress:

$$\sigma_{eff} = P_a/(1-V_p^{2/3}) \qquad (4\text{-}8),$$

where V_p is the volume fraction porosity. Spriggs <u>et al</u>. (1964) suggested that the effective stress in a crystalline material could be better expressed by

$$\sigma_{eff} = P_a(1+2V_p) \qquad (4\text{-}9).$$

This expression is an adaptation from the experimental and theoretical changes in elastic modulus with porosity. Farnsworth and Coble (1966) introduced the relation:

$$\sigma_{eff} = P_a/D \qquad (4\text{-}10).$$

where D is the relative density, for the evaluation of the strain rate in polycrystalline silicon carbide; while Rao and Chaklader (1972) suggested that the stress effectively causing deformation in a porous polycrystalline solid could be computed from the deformational geometries of the particles in contact. They proposed that under a uniaxial load, the effective stress can be calculated if it is assumed that the particles, being deformed at the points of contact, are monosized spheres with an assumed packing geometry. The resulting expression is

$$\sigma_{eff} = \sigma/[\alpha_1(D^{2/3}\beta^{2/3}R^2 - 1)] \qquad (4\text{-}11),$$

where α_1 and β are geometric constants whose values depend on the packing geometry; and R is the particle radius.

All the formulations for σ_{eff} suggested above are plotted as a function of D in Figure 4-1. The curves labelled "bcc", "ortho", "rhomb", and "cubic" correspond to the packing symmetries of the quasi-spherical model proposed by Rao and Chaklader (1972). Even though the expressions given for the effective stress in Equations 4-8 through 4-10 are different, the values of the effective stress at a particular density are almost equivalent. The values of the effective stress calculated from Equation 4-10, on the other hand, differ greatly from those computed from the other expressions.

Coble (1970) considered the formulations for effective stress proposed by McClelland (1964), Spriggs <u>et al</u>. (1964) and Farnsworth and Coble (1966) -- Equations 4-8 through 4-10 -- and concluded that the effective stress in the grain boundary should not include a stress concentration factor, σ_{eff}/σ, due to porosity because both the stress distribution on the grai boundary and the concentration distribution of defects along the grain boundary must satisfy the diffusion equation. Hence he suggested that only the form of the effective stress given by Equation 4-10 is acceptable for intermediate to final stage hot-pressing. Coble however did not consider Equation 4-11. As can be seen in Figure 4-1, the stress concentration factor predicted by Equation 4-11 for each of the packing geometries is much higher than that predicted by Equation 4-10. In the next section we will compare the densification rates predicted by both of these formulations with the densification rates obtained from the experimental data to determine which of the formulations gives

Figure 4-1

Variation of the stress intensity factor, σ_{eff}/σ_{ob}, with relative density, D. The curves have been derived from the various models proposed for the effective stress, σ_{eff}, causing deformation during hot-pressing. These models are:

(a) McClelland (1964): $\sigma_{eff}/\sigma_a = (1-Vp^{2/3})^{-1}$

where p = 1-D.

(b) Spriggs et al. (1964): $\sigma_{eff}/\sigma_a = (1+2Vp)$

(c) Farnsworth and Coble (1966): $\sigma_{eff}/\sigma_a = 1/D$

(d) Rao & Chaklader (1972):

$\sigma_{eff}/\sigma_a = [\alpha_1(D^{2/3}\beta^{2/3}R^2-1)]^{-1}$ where α_1 and β are geometric constants whose values depend upon the packing model assumed; and R is the particle radius. They suggest that the stress effectively causing deformation in a porous polycrystalline solid can be computed from the deformational geometries of the particles in contact. The four packing geometries assumed are cubic, orthorhombic, bcc and rhombohedral.

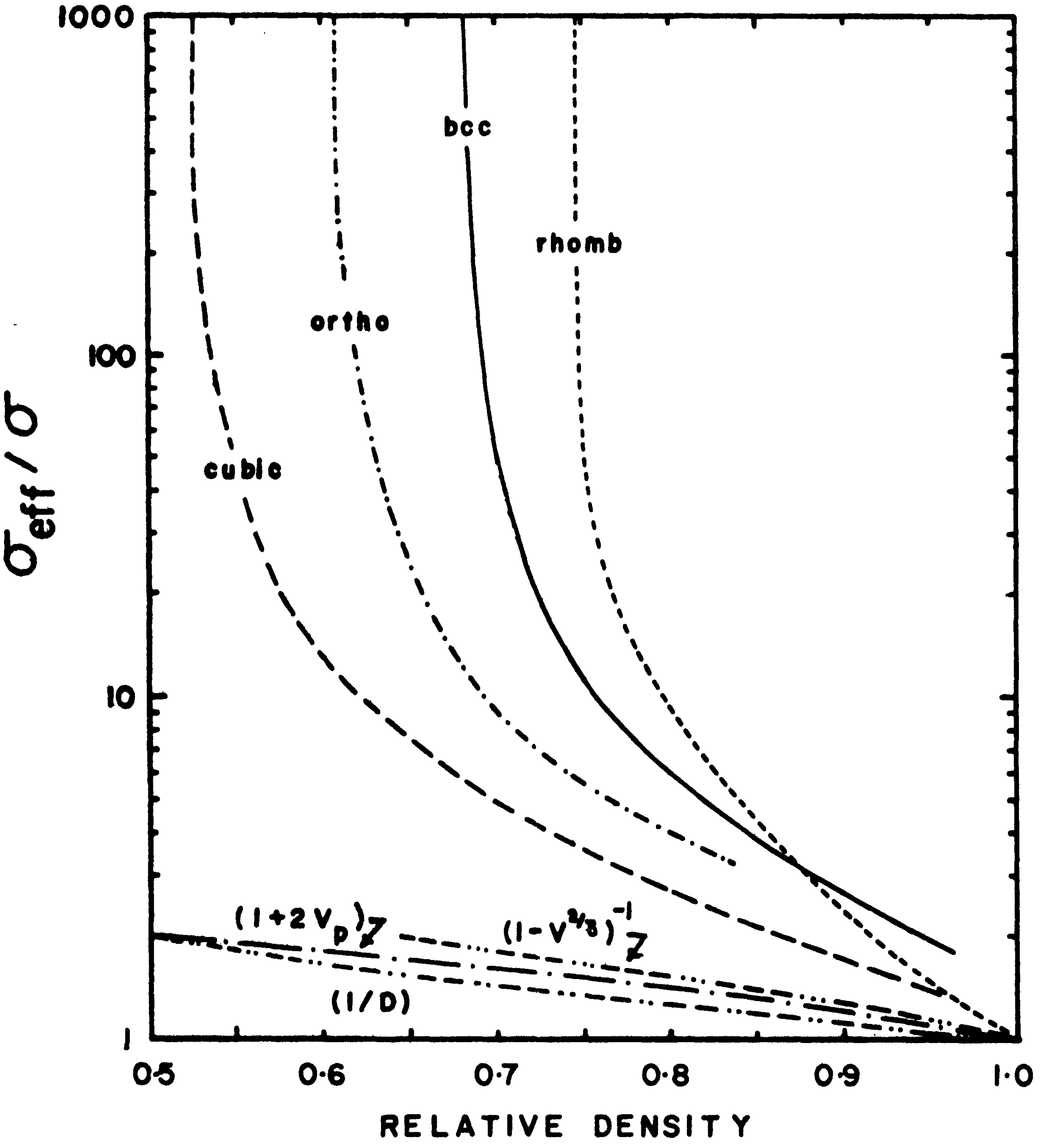1000
100
10
1
0·5
0·6
0·7
0·8
0·9
1·0
RELATIVE DENSITY
σ_{eff} / σ
bcc
rhomb
ortho
cubic
$(1+2V_p)$
$(1-V^{2/3})^{-1}$
(1/D)

FIGURE 4-1

more consistent results.

<u>Comparison of the predicted densification rates using the effective stress models with the experimentally determined densification rates</u>. The difficulty in using the dense flow laws to predict the behavior of a material for given σ, T, and grain size conditions is that we often do not have data for Coble creep, power-law creep, and so forth. For olivine, we have data for the power-law field but not for the Coble field. Wilkinson and Ashby (1975); however, have assembled the existing theories for densification during hot-pressing, such as the Coble creep equation:

$$\dot{\varepsilon} = A_c \sigma \exp(-Q_{Coble}/RT) G^{-3} \qquad (4\text{-}12),$$

and have provided parameters for the Coble field:

$$Q_{Coble} = \frac{2}{3} Q_{\text{Power-law creep}} \qquad (4\text{-}13a),$$

and

$$A_c = \frac{47.5 D_b \Omega w}{kT} \qquad (4\text{-}13b),$$

where none have been determined experimentally. Using these rules of thumb for the Coble field and the various effective stress formulations proposed by Coble (1970), Rao and Chaklader (1975), and so forth, the densification rates predicted for the Coble and power-law creep fields can be derived. These densification rates are plotted as a function of grain size in Figure 3-8.

For the finer-grain-sized powders, the predicted densification curves follow the same trend as the curve which "best-fits" the hot-pressing data; but the absolute strain rates provided by all models are too slow. We cannot compare the predicted curves with the experimental curve at the coarser-grain sizes, however, since the sharp change in grain-size sensitive is not observed for our hot-pressed specimens. We believe that the presence of a large proportion of fine-grained particles in the coarse-grained specimens ($G > 53\mu m$) tends to smear out the effect of grain size on creep.

We can adjust the Coble parameters (Equations 4-13) provided by Ashby to make the predicted curves fit our observations. Using the activation energy, $Q = 85$ kcal/mole, determined for our hot-pressed specimens as the value of Q_{Coble}, the value of A_C in Equation 4-12 which brings each of the predicted curves into agreement with the "best-fit" curve can be determined.

4.2 The Transition to Grain Size Insensitive Creep

We have picked an effective stress at 15% porosity from the middle of the range of values given in Figure 4-1. The effective stress chosen is $\sigma_{eff} = 2\sigma_{applied}$. Using this value for the effective stress, an activation energy of 85 kcal/mole, and the experimental parameters given in Figure 3-8 -- Log $\dot{\varepsilon} = -2.70$, $G = 10\mu m$, $T = 1429°C$, and $\sigma = 166$ bars -- we have determined that the value of the Coble parameter in Equation 4-12 is $5 \times 10^{-4} cm^3$/bar-sec. This parameter allows us to predict the grain size at which the transition to grain-size insensitive creep occurs. We compute this grain size to be 129μm at 1429°C and 166 bars (the power-law creep parameters used are Q_{PLC} = 125 kcal/mole, A_{PLC} = 290 bar^{-3}-sec^{-1}, and n = 3).

The Coble parameters we have just obtained also allow us to predict the transition in the mantle from Coble to power-law creep. We have used the Q_c and A_c determined from our data and the power-law creep parameters given above, to correct the Ashby deformation map (Stocker and Ashby, 1973). For the upper mantle, grain size 1mm. The field boundaries determined using the Coble parameters given in Equations 4-13 (values of D_b, Ω, etc. given in Stocker and Ashby, 1973) are shown as heavy dashed lines in Figure 4-2; while the field boundaries determined using the Q_c and A_c from our data, as heavy, solid lines. As a result of the modification of the deformation map, the Coble field has expanded slightly, and the power-law and Nabarro-Herring fields, shrunk, in comparison with previous estimates.

It is instructive to trace a particular strain rate contour across the deformation map; in this case, the $10^{-15}sec^{-1}$ contour. Using this contour, we compute the transition from Coble to power-law creep in the upper mantle. For a grain size of 1mm and a strain rate of $10^{-15}sec^{-1}$, the transition occurs at 794°C and 514 bars. However, this transition will occur at 779°C and 656 bars if the stress exponent in Equation 4-12 is 1.5 instead of 1.0. The transition to grain-size insensitive creep for strain rates of $10^{-15}sec^{-1}$ and $10^{-13}sec^{-1}$ has also been computed for several other grain sizes using the Coble parameters (Q = 85 kcal/mole, and $A_c = 5x10^{-4}cm^3$/bar-sec) and the power-law creep

Figure 4-2

A deformation map for the upper mantle is plotted assuming that $P = 10$ kb., $V^* = 20\text{X}10^{-24}$ cm^3, and $G = 1$ mm. The rate equations used to compute the field boundaries are those given by Stocker and Ashby (1973). To obtain the field boundaries (heavy lines) between various deformation mechanisms, activation energies equal to 85 kcal/mole for Coble creep and 125 kcal/mole for power-law creep were assumed; and the constant, $A_{coble}=5.0\text{X}10^{-4}$ cm^3/bar-sec, in Equation 4-12 was used. For comparison, the field boundaries obtained using Ashby's rules of thumb (Equations 4-13) are plotted in the figure as the heavy dashed lines. A strain rate contour at 10^{-15} sec^{-1} is also shown on the figure as a thin line. Using this contour, the temperature and stress at which the transition to grain size insensitive creep occurs can be obtained.

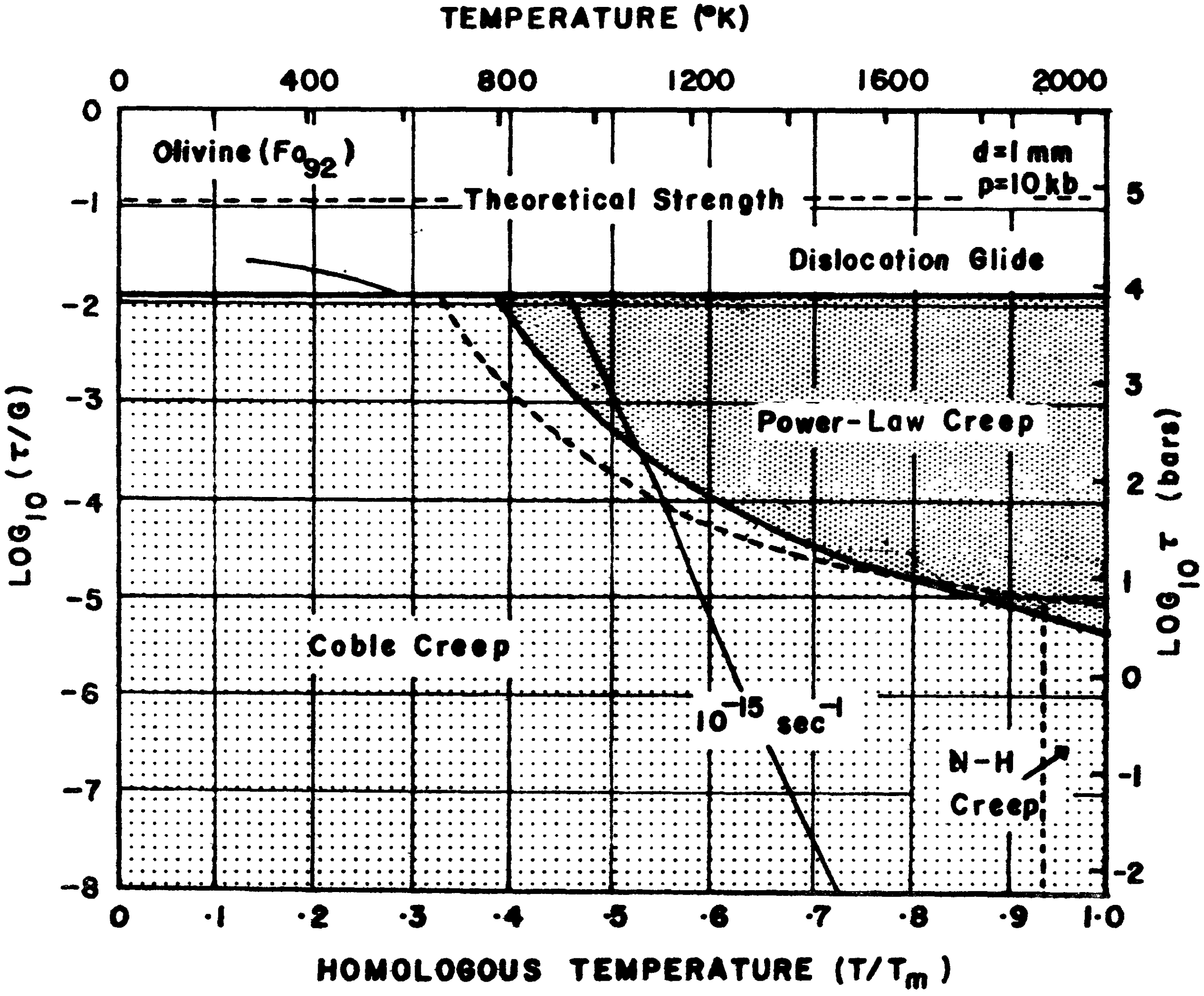
TEMPERATURE (°K)
0
400
800
1200
1600
2000
Olivine (Fo_{92})
d=1 mm
p=10 kb
Theoretical Strength
Dislocation Glide
Power-Law Creep
Coble Creep
10^{-15} sec^{-1}
N-H Creep
LOG$_{10}$ (τ/G)
0
-1
-2
-3
-4
-5
-6
-7
-8
LOG$_{10}$ τ (bars)
5
4
3
2
1
0
-1
-2
0
·1
·2
·3
·4
·5
·6
·7
·8
·9
1·0
HOMOLOGOUS TEMPERATURE (T/T$_m$)

FIGURE 4-2

parameters given above. The results are tabulated in Table 4-1.

4.3 The Effect of Hydrogen Fugacity

There is an indication in our hot-pressed data that hydrogen fugacity has a minor effect on the strain rate, c.f. Section 3.6, that is, the strain rates obtained for aggregates deformed in a CO_2/H_2 atmosphere are faster than those obtained from tests conducted in a CO_2/CO atmosphere. The variation of strain rate with the atmosphere used is evident in Figure 3-9 in which strain rates obtained for 25-53μm specimens in both atmospheres are plotted.

This result could be interpreted through the "water-weakening" effect of Blacic (1972) and Carter and Ave-Lallemant (1970), i.e., it might cause the individual crystals to deform more readily by intracrystalline slip. Alternatively, moisture could affect the surface diffusivities and therefore the deformation rate through a Coble mechanism.

TABLE 4-1

TRANSITION FROM COBLE CREEP TO POWER-LAW CREEP

$Q_C = 85$ kcal/mole
$n = 1.0$
$A_C = 5\mathrm{x}10^{-4}\mathrm{cm}^3/\mathrm{bar}\text{-}\mathrm{sec}$

$Q_{PLC} = 125$ kcal/mole
$n = 3$
$A_{PLC} = 2.9\mathrm{x}10^{2}\mathrm{bar}^{-3}\cdot\mathrm{sec}^{-1}$

	$\dot{\varepsilon} = 10^{-15}\mathrm{sec}^{-1}$		$\dot{\varepsilon} = 10^{-13}\mathrm{sec}^{-1}$	
T(°C)	$\sigma_1-\sigma_3$(bars)	G(cm)	$\sigma_1-\sigma_3$(bars)	G(cm)
700	3470	0.05		
800	462	0.104	2100	0.037
1000	21.6	0.30	100	0.11
1200	2.3	0.65	11	0.24
1400	0.42	1.17	1.9	0.42

$Q_C = 85$ kcal/mole
$n = 1.5$
$A_C = 2.7\mathrm{x}10^{-5}\mathrm{cm}^3/\mathrm{bar}\text{-}\mathrm{sec}$

$Q_{PLC} = 125$ kcal/mole
$n = 3$
$A_{PLC} = 2.9\mathrm{x}10^{2}\mathrm{bar}^{-3}\cdot\mathrm{sec}^{-1}$

	$\dot{\varepsilon} = 10^{-15}\mathrm{sec}^{-1}$		$\dot{\varepsilon} = 10^{-13}\mathrm{sec}^{-1}$	
	$\sigma_1-\sigma_3$(bars)	G(cm)	$\sigma_1-\sigma_3$(bars)	G(cm)
700	3297	0.08		
800	444	0.107	2067	0.05
1000	20.8	0.19	97	0.09
1200	2.2	0.28	10.4	0.13
1400	0.41	0.38	1.9	0.18

CHAPTER V

CONCLUSIONS

(1) The relative density, D, versus elapsed time curves for hot-pressed olivine (Fo_{92}) are as shown in Figure 3-4 for grain sizes in the range from 1 to 2000 μm, temperatures in the range of 1000° to $1650^{\circ}C$, and stresses in the range of 100 to 400 bars.

(2) For dense fine-grained aggregates ($G<25$ μm), the average stress exponent, n, is 1.5±0.4; while for the medium-grained aggregates tested (25-250μm) the average value of n is 3.4±0.8. The activation energy obtained for our hot-pressed specimens is 85±29 kcal/mole. The strain rate for the fine-grained aggregates varies approximately as the third power of the grain size; but the grain size dependence of the strain rate for the medium- to coarse-grained aggregates is masked by the presence of fines in these aggregates.

(3) In our hot-pressed specimens, all grains, both coarse and fine, deform plastically. In addition, the coarse grains fracture; the fine grains do not. The densification of the coarse-grained powders is aided by the densification of the fine-grain-sized particles in these specimens.

(4) There is an indication in our data that the effect of oxygen fugacity on strain rate is unimportant. Hydrogen fugacity, on the other hand, appears to have a minor effect, i.e., it "softens" olivine.

(5) Uncertainities in the formulation for the effective stress, σ_{eff}, impair the direct translation of hot-pressing data into dense flow laws.

(6) Using an activation energy of 85 kcal/mole for Coble creep, and the A determined from the hot-pressing data for the fine-grained aggregates, the Stocker-Ashby (1973) deformation map for the upper mantle has been modified, and the stress and temperature conditions appropriate for several grain sizes at a strain rate of 10^{-15} sec^{-1}, obtained. As a result of the modification of the deformation map, the Coble field is expanded slightly and the power-law creep field, shrunk, in comparison with previous estimates.

APPENDIX A

AN ESTIMATE OF THE SURFACE ENERGY AND THE DRIVING FORCE DUE TO SURFACE ENERGY

A.1 An Estimate of the Surface Energy of Olivine

A rough estimate of the surface energy, γ, can be obtained from the elastic constants of a crystal (Gilman, 1960; Brace and Walsh, 1962) if it is assumed that the force acting across any surface can be represented by a sine function. The force is zero both at the atomic radius of the atom and when the atoms across the plane have their normal separation. Hence the surface free energy for a crystal can be estimated from the expression (Gilman, 1960, p.2216):

$$\gamma = \frac{E a^2}{d_o \pi^2} \qquad \text{(A-1)},$$

where a is the atomic radius of atoms across the plane; d_o, the spacing of the planes; and E, Young's modulus normal to the plane in question. Brace and Walsh (1962) calculated the value of the surface energy for olivine (Fo_{92}) by assuming that the Si tetrahedra remain intact during cleavage and that the value of 'a' equals the average of the Mg and O radii. They determined the theoretical value for the surface energy, γ, of olivine to be 370 erg/cm^2. The specific surface energy of the common minerals, excluding feldspar, ranges from about 100 to 2000 erg/cm^2 (Brace and Walsh, 1962).

A.2 Driving Force Due to Surface Energy

Coble (1970) suggests that the radii of closed pores during the final stage of densification can be approximated by the relation:

$$r = (1-D)^{1/3} (G/2) \qquad \text{(A-2)}$$

where r is the pore radius in cm; D, the relative density of the specimen; G, the grain size in cm. For a dense hot-pressed specimen with D = 0.99 (%ϕ = 1%) and a mean grain size of 7μm, the theoretical pore radius would be 0.75μm. Similarly for dense (D = 0.99) hot-pressed specimens with mean grain sizes 25μm and 50μm, the theoretical pore radii would be 2.7μm and 16.2μm, respectively.

Consequently, the driving force due to surface energy during final-stage hot-pressing, given by $2\gamma/r$ will be negligible compared to the applied stress. That is, for the dense 7μm specimen considered above (D = 0.99). The driving force due to surface energy will be 9.9 bars, or about 10% of the applied stress, σ_a, at σ_a = 100 bars and 5% at σ_a = 200 bars. Similarly, the driving force due to surface energy for the 25μm dense specimen will be only 2.8 bars or about 3% of the applied stress, at σ_a = 100 bars; while for the 150μm specimen, only 0.5% of the applied stress at σ_a = 100 bars.

APPENDIX B

DATA TABLES

Data from the hot-pressing experiments listed in Table 3-1 presented and reduced on the following pages. For all runs, the following symbols and equations apply:

(a) Symbols:

h_o = initial specimen height (in.)

h_o-h_s = specimen height at time load is applied (in.)

r = specimen radius, constant for each run (in.)

M = mass of specimen (gm)

G = grain size fraction (μm)

T = temperature (°C)

σ_a = applied load (bars)

D = relative density of specimen

ϕ = porosity

$\dot{\varepsilon}$ = strain rate ($\sec^{-1}$)

(b) Equations:

(1) Hot-pressing equation (Coble, 1970):

$$\dot{\varepsilon} = -\frac{1}{h}\frac{dh}{dt}$$

(2) Relative density:

D = (actual density/theoretical single-crystal density),

where theoretical single crystal density = 3.373 gm/cm^3;

(3) Porosity:

$\phi = 1-D.$

(4) Time:

Δt = time interval (sec.)

total t = time elapsed from application of load

S-1

G = 25 μm and less (bimodal)

$h_o = 0.211$ $h_o - h_s = 0.209$ $r = 0.125$ $M = 0.3964$

σ and T	Δt	total t	h	D	%ϕ	$-(\text{Log } \dot{\varepsilon})$
166 bars,						
1000°						
	40.8	41	.208	.702	29.8	3.88
	120.0	161	.207	.706	29.4	4.35
	120.0	281	.206	.710	29.1	4.46
	120.0	401	.205	.712	28.8	4.52
	120.0	521	.205	.714	28.6	4.60
	120.0	641	.204	.716	28.4	4.69
	511.4	1224	.202	.723	27.7	4.78
	360.0	1584	.201	.727	27.3	4.86
	360.0	1944	.200	.730	27.0	4.99
	360.0	2664	.199	.734	26.6	5.06
	259.2	3283	.198	.737	26.3	5.14
1234°						
	6.0	6	.195	.748	25.2	2.62
	12.0	18	.192	.760	24.0	2.90
	12.0	30	.191	.768	23.2	3.06
	12.0	42	.189	.774	22.6	3.19
	12.0	54	.188	.779	22.1	3.22
	12.0	66	.187	.784	21.6	3.30
	12.0	78	.185	.788	21.2	3.35

S-1, cont'd.

σ and T	Δt	total t	h	D	%ϕ	-(Log $\dot{\varepsilon}$)
	12.0	102	.184	.796	20.4	3.41
	12.0	114	.183	.799	20.1	3.47
	12.0	126	.182	.802	19.8	3.47
	12.0	150	.181	.808	19.2	3.54
	12.0	174	.180	.813	18.7	3.64
	71.5	258	.177	.827	17.3	3.67
	60.0	318	.175	.836	16.4	3.78
	60.0	378	.174	.843	15.7	3.89
	60.0	438	.172	.849	15.5	3.92
	60.0	498	.171	.854	14.6	3.97
	60.0	558	.170	.859	14.2	4.07
	319.2	937	.165	.885	11.5	4.11
	360.0	1297	.163	.899	10.1	4.36
	360.0	1657	.161	.909	9.1	4.50
	360.0	2017	.159	.918	8.2	4.59
	360.0	2377	.158	.926	7.4	4.62
	720.0	3097	.156	.936	6.4	4.82
	432.0	3817	.155	.944	5.6	4.96
	360.0	4177	.154	.948	5.3	5.05
	360.0	5257	.153	.956	4.4	5.20
	360.0	5617	.153	.957	4.3	5.61
	360.0	7417	.153	.959	4.2	6.34

S-2

G = 20-25 μm

$h_o = 0.187$ $h_o - h_s = 0.170$ $r = 0.127$ $M = 0.3824$

σ and T	Δt	total t	h	D	%φ	-(Log $\dot{\varepsilon}$)
166 bars, 1565°						
	.2	.4	.167	.790	21.0	1.38
	.2	.6	.166	.797	20.3	1.40
	.2	.8	.165	.800	20.0	1.70
	.2	1.2	.164	.805	19.5	1.79
	.2	1.6	.163	.809	19.1	1.95
	.2	2.0	.163	.811	18.9	2.39
	2.0	7.3	.162	.818	18.2	2.81
	2.0	9.3	.161	.820	18.0	2.91
	16.7	28.6	.159	.834	16.6	3.06
	19.2	46.8	.156	.847	15.3	3.09
	24.0	70.7	.154	.858	14.2	3.26
	24.0	94.8	.152	.868	13.2	3.34
	24.0	199	.151	.876	12.4	3.41
	24.0	143	.150	.884	11.6	3.42
	24.0	167	.148	.891	10.9	3.50
	147.9	317	.144	.920	8.1	3.68
	120.0	437	.141	.936	6.4	3.83
	120.0	557	.139	.948	5.2	3.97
	120.0	677	.138	.957	4.3	4.12
	120.0	797	.137	.960	4.0	4.58

S-2, cont'd.

σ and T	Δt	total t	h	D	%ϕ	$-(\text{Log } \dot{\varepsilon})$
	120.0	1157	.136	.970	3.0	4.61
	120.0	1877	.135	.982	1.8	4.99

S-3

G = 105-250

$h_o = 0.241$ $h_o - h_s = 0.235$ $r = 0.122$ $M = 0.4374$

σ and T	Δt	total t	h	D	%ϕ	$-(\mathrm{Log}\ \dot{\varepsilon})$
166 bars, 1469°						
	6.2	6	.231	.739	26.2	2.49
	9.6	16	.227	.749	25.1	2.83
	24.0	40	.223	.764	23.6	3.00
	24.0	64	.221	.772	22.8	3.33
	24.0	88	.219	.778	22.2	3.49
	24.0	112	.217	.783	21.7	3.56
	24.0	136	.216	.788	21.2	3.60
	24.0	160	.215	.791	20.9	3.72
	24.0	184	.214	.795	20.5	3.75
	24.0	232	.213	.800	20.0	3.89
298 bars	3.8	262	.211	.806	19.4	3.19
	5.8	271	.210	.811	18.9	3.27
	5.8	277	.209	.813	18.7	3.33
	6.2	283	.209	.815	18.5	3.40
200 bars	5.3	288	.209	.815	18.5	3.93
	24.0	408	.208	.818	18.1	4.28
	24.0	480	.207	.823	17.7	4.10
	114.2	618	.205	.831	16.9	4.18

S-3, cont'd.

σ and T	Δt	total t	h	D	%φ	$-(\text{Log }\dot{\varepsilon})$
	24.0	762	.203	.839	16.9	4.27
	96.0	858	.202	.844	15.6	4.33
	120.0	1098	.201	.852	14.8	4.41
	120.0	1338	.198	.860	14.0	4.48
	352.8	1691	.196	.867	13.3	4.61
	360.0	2051	.195	.872	12.8	4.78
	360.0	2411	.194	.876	12.4	4.95
298 bars						
	100.8	2627	.192	.889	11.1	3.85
	144.0	2771	.190	.896	10.5	4.28
	144.0	2915	.189	.900	10.0	4.54
	216.0	3131	.188	.904	9.6	4.65
	144.0	3275	.188	.906	9.4	4.92

S-4

G = 25-53 (CO_2/H_2)

$h_o = 0.142$ $h_o - h_s = 0.141$ $r = 0.124$ $M = 0.2668$

σ and T	Δt	total t	h	D	%ϕ	$-(\text{Log } \dot{\varepsilon})$
166 bars, 1465°						
	4.8	6	.131	.734	23.4	1.86
	12.0	18	.130	.767	23.3	3.05
	12.0	30	.129	.774	22.6	3.24
	12.0	42	.128	.779	22.1	3.28
	19.2	65	.126	.787	21.3	3.25
	49.4	115	.125	.797	20.3	3.59
	60.0	175	.123	.808	19.2	3.67
	60.0	235	.122	.817	18.3	3.79
	60.0	295	.121	.824	17.6	3.86
	60.0	355	.120	.831	16.9	3.90
	60.0	415	.119	.837	16.0	3.95
	60.0	475	.118	.842	15.8	4.01
	48.0	523	.118	.846	15.4	4.05
	60.0	655	.117	.856	14.4	4.15
	60.0	895	.115	.870	13.0	4.24
	60.0	1135	.113	.883	11.7	4.36
	120.0	1711	.110	.904	9.4	4.52
	120.0	1951	.110	.910	9.0	4.64

S-4, cont'd.

σ and T	Δt	total t	h	D	%ϕ	$-(\text{Log }\dot{\varepsilon})$
	120.0	2071	.109	.912	8.8	4.82
	360.0	3100	.108	.925	7.5	5.11
	360.0	3820	.107	.930	7.0	5.29

S-5

G = 1000-2000

h_o = 0.098 $h_o - h_s$ = 0.098 r = 0.125 M = 0.1901

σ and T	Δt	total t	h	D	%ϕ	$-(\text{Log } \dot{\varepsilon})$
166 bars, 1430°						
	7.7	8	.096	.730	27.0	2.74
	6.2	14	.095	.741	25.9	2.60
	12.0	26	.094	.747	25.3	3.18
	12.0	50	.093	.753	24.7	3.48
	36.0	207	.091	.767	23.3	3.95
	360.0	1009	.090	.781	21.9	4.72
	360.0	2449	.089	.787	21.3	5.51

S-7

G = 250-500

$h_o = 0.105$ $\dot{h}_o - h_s = 0.105$ $r = 0.125$ $M = 0.2025$

σ and T	Δt	total t	h	D	%φ	$-(\text{Log } \dot{\varepsilon})$
166 bars, ~1430°						
	21.8	29	.103	.722	27.8	3.42
	12.0	41	.103	.725	27.5	3.52
	12.0	77	.102	.731	26.9	3.69
	12.0	137	.101	.737	26.3	3.88
	82.6	265	.100	.745	25.5	4.13
	60.0	325	.099	.753	24.7	4.38
	60.0	805	.098	.759	24.1	4.68
	364.8	1544	.097	.768	23.2	4.86
	360.0	2624	.096	.779	22.1	4.97

S-9

G = 1000-2000

$h_o = 0.096$ $h_o - h_s = 0.094$ $r = 0.125$ $M = 0.1892$

σ and T	Δt	total t	h	D	%ϕ	−(Log $\dot{\varepsilon}$)
166 bars, 1587°	1.4	1.4	.093	.750	25.0	2.19
	9.6	11	.091	.767	23.3	2.63
	24.0	35	.090	.780	22.0	3.20
	60.0	167	.089	.791	20.9	3.93
	60.0	407	.087	.798	20.2	4.33
	360.0	1497	.086	.816	18.4	4.70
	360.0	2211	.085	.823	17.7	5.09
	360.0	3291	.084	.830	17.0	5.39
	360.0	4371	.084	.834	16.6	5.39

S-11

G = 250-500

$h_o = 0.150$ $h_o - h_s = 0.150$ $r = 0.125$ $M = 0.2999$

σ and T	Δt	total t	h	D	%ϕ	$-(\text{Log } \dot{\varepsilon})$
166 bars, ~1594°						
	25.0	25	.147	.753	24.7	3.08
	24.0	49	.146	.760	24.0	3.41
	24.0	73	.145	.764	23.6	3.67
	24.0	97	.144	.766	23.4	3.54
	24.0	169	.143	.772	22.8	3.67
	24.0	265	.142	.778	22.2	4.14
	60.0	446	.141	.786	21.4	4.23
	60.0	686	.140	.793	20.7	4.35
	327.6	1074	.138	.804	19.6	4.48
	360.0	1434	.137	.811	18.9	4.65
	360.0	1794	.136	.816	18.4	4.75
	360.0	2154	.135	.825	17.5	4.81
	360.0	2874	.134	.828	17.2	4.89
	360.0	3234	.133	.832	17.8	4.99
	360.0	4314	.132	.842	15.8	5.10
	360.0	5394	.131	.848	15.2	5.58

S-12

G = 500-1000

$h_o = 0.112$ $h_o - h_s = 0.112$ $r = 0.125$ $M = 0.2181$

σ and T	Δt	total t	h	D	%ϕ	$-(\text{Log}\ \dot{\varepsilon})$
166 bars, 1600°	22.6	23	.110	.735	26.6	3.05
	24.0	47	.109	.740	26.1	3.55
	24.0	71	.108	.742	25.8	3.85
	55.0	126	.108	.746	25.4	3.98
	60.0	186	.107	.751	24.9	4.02
	60.0	245	.107	.754	24.6	4.11
	60.0	426	.105	.764	23.6	4.23
	60.0	666	.104	.774	22.6	4.40
	226.8	1122	.102	.790	21.0	4.43
	360.0	1492	.101	.796	20.4	4.69
	360.0	1852	.100	.801	19.9	4.77
	360.0	2572	.099	.809	19.1	4.98
	360.0	4372	.098	.821	17.9	5.45
	360.0	7972	.097	.829	17.1	5.45

S-13

G = 5-10

h_o = 0.085 $h_o - h_s$ = 0.074 r = 0.0313 M = 0.0093

σ and T	Δt	total t	h	D	%φ	$-(\text{Log}\ \dot{\varepsilon})$
149 bars, ~1284°						
	1.8	2	.069	.769	23.1	1.41
	2.0	4	.068	.802	19.8	2.29
	2.0	8	.067	.813	18.7	2.53
	8.5	20	.066	.825	17.5	2.91
	12.0	32	.065	.835	16.5	2.98
	49.9	82	.064	.851	14.9	3.30
	60.0	142	.063	.868	13.2	3.58
	60.0	202	.062	.880	12.0	3.75
	445.2	647	.060	.901	9.9	4.08
	360.0	1007	.059	.925	7.3	4.39
	360.0	1367	.058	.936	6.4	4.60
	360.0	2447	.057	.955	4.6	4.84
	360.0	3527	.057	.965	3.5	5.09
	360.0	4607	.056	.973	2.7	5.18
	360.0	5327	.056	.977	2.3	5.31
	360.0	6767	.056	.982	1.8	5.48
	360.0	8207	.056	.987	1.3	5.78
	360.0	9287	.056	.989	1.1	5.78

S-14

G = 5-10

h_o = 0.158 h_o-h_s = 0.157 r = 0.124 M = 0.2597

σ and T	Δt	total t	h	D	%φ	-(Log $\dot{\varepsilon}$)
110 bars 1008°						
	26.4	26	.156	.624	37.6	4.01
	91.2	160	.156	.626	37.4	4.85
177 bars						
	7.2	181	.156	.627	37.3	3.53
	5.3	199	.154	.633	36.7	4.39
	148.8	348	.154	.635	36.6	4.72
350 bars						
	139.2	487	.153	.637	36.3	4.60
	489.6	1227	.152	.643	35.7	4.78
110 bars 1120°						
	201.6	1444	.150	.650	35.0	4.28
	360.0	1804	.148	.659	34.1	4.43
	266.4	2070	.147	.665	33.5	4.52
210 bars						
	10.3	2094	.147	.666	33.4	3.88
	14.2	2108	.146	.666	33.4	4.10
	309.6	2418	.145	.675	32.5	4.41
	144.0	2562	.144	.678	32.3	4.52
	360.0	2922	.143	.683	31.7	4.62

S-14, cont'd.

σ and T	Δt	total t	h	D	$\%\phi$	$-(\text{Log } \dot{\varepsilon})$
110 bars 1230°						
	93.6	3015	.141	.690	31.0	3.97
	93.6	3109	.139	.702	29.8	3.74
	72.0	3253	.136	.720	28.0	3.78
	144.0	3397	.132	.737	26.3	3.80
	216.0	3613	.129	.756	24.4	3.95
	360.0	3973	.126	.777	22.3	4.12
	144.0	4117	.125	.784	21.6	4.24
177 bars						
	216.0	4333	.123	.795	20.5	4.18
	360.0	4693	.121	.810	19.0	4.30
	360.0	5053	.119	.822	17.8	4.37
	367.2	5420	.117	.832	16.7	4.48
110 bars 1334°						
	129.6	5550	.116	.842	15.8	4.06
	194.4	5744	.111	.872	12.8	3.75
	144.0	5888	.110	.889	11.1	3.86
	216.0	6104	.107	.913	8.7	3.92
	352.8	6457	.104	.938	6.2	4.11
177 bars						
	360.0	6817	.102	.961	4.0	4.19
	360.0	7177	.100	.975	2.5	4.39
	144.0	7321	.100	.979	2.1	4.52

S-14, cont'd.

σ and T	Δt	total t	h	D	%ϕ	$-(\text{Log } \dot{\varepsilon})$
210 bars						
	18.7	7340	.099	.984	1.6	3.60
	266.4	7606	.098	.993	0.7	4.44
	360.0	7966	.098	.998	0.1	4.84

S-15

G = 1000-2000

h_o = .149 h_o-h_s = 0.148 r = 0.120 M = .02785

σ and T	Δt	total t	h	D	%φ	-(Log $\dot{\varepsilon}$)
291 bars						
	.5	1.0	.146	.754	24.6	1.67
	.7	2.0	.144	.762	23.8	1.80
	1.0	2.4	.143	.771	22.9	1.94
	7.4	9.8	.138	.788	21.3	2.38
	12.0	22.0	.135	.809	19.1	2.71
	12.0	33.0	.134	.823	17.7	3.06
	12.0	46.0	.133	.830	17.0	3.20
	16.8	63.0	.132	.837	16.4	3.38
	24.0	120.0	.130	.849	15.1	3.59
	24.0	144.0	.129	.853	14.7	3.69
	24.0	168.0	.129	.857	14.3	3.79
	21.1	189.0	.128	.860	14.0	3.83
	82.8	272.0	.127	.865	13.5	3.98
	60.0	332.0	.127	.871	12.9	4.04
	60.0	392.0	.126	.876	12.5	4.15
	81.6	474.0	.126	.880	12.0	4.21
	81.6	555.0	.125	.884	11.6	4.23
	192.0	747.0	.124	.890	11.0	4.31
	259.2	1006.0	.123	.898	10.2	4.46
	360.0	1367.0	.121	.908	9.3	4.51
	360.0	1727.0	.120	.917	8.3	4.54

S-15, cont'd.

σ and T	Δt	total t	h	D	%φ	-(Log $\dot{\varepsilon}$)
291 bars (cont'd.)						
	288.0	2015.0	.119	.925	7.5	4.69
	432.0	2447.0	.118	.931	6.9	4.74
	432.0	2879.0	.118	.938	6.3	4.91
	288.0	3167.0	.117	.941	5.9	5.10
	360.0	3527.0	.117	.943	5.7	5.20
	360.0	4247.0	.117	.947	5.3	5.40
	360.0	4967.0	.116	.950	5.0	5.50
	720.0	6407.0	.116	.953	4.7	5.55

S-16

G = 20-25

h_o = 0.187 $h_o - h_s$ = 0.175 r = 0.120 M = 0.3057

σ and T	Δt	total t	h	D	%ϕ	$-(\text{Log } \dot{\varepsilon})$
291 bars						
1008°						
	1.4	1	.174	.707	29.4	2.88
	3.1	5	.174	.708	29.2	3.53
	120.0	147	.173	.710	29.0	4.75
	112.8	260	.173	.711	28.9	5.07
110 bars						
1157°						
	396.0	656	.172	.714	28.6	4.76
291 bars						
1176°						
	1.4	658	.172	.717	28.3	2.72
	1.0	659	.171	.719	28.1	3.00
	21.6	680	.171	.720	28.0	3.87
	1.7	682	.171	.721	27.9	3.94
	115.2	797	.170	.724	27.6	4.23
	295.2	1092	.169	.729	27.1	4.63
110 bars						
1245°						
	186.0	1494	.164	.750	25.1	3.91
	90.0	1584	.163	.755	25.5	4.06
1305°						
	68.4	1653	.162	.760	24.0	4.11
	7.4	1667	.161	.764	23.6	4.26

S-16, cont'd.

σ and T	Δt	total t	h	D	%ϕ	$-(\text{Log } \dot{\varepsilon})$
176 bars						
1305°						
	31.7	1826	.160	.767	23.3	3.67
	15.8	2021	.159	.773	22.7	3.98
	133.2	2155	.158	.778	22.2	4.09
291 bars						
1305°						
	25.7	2180	.157	.784	21.6	3.65
	134.4	2315	.154	.794	20.6	3.86
	273.6	2790	.149	.819	18.1	4.16
1176°						
	20.9	2811	.149	.827	17.4	4.97
110 bars						
1305°						
	564.0	3466	.148	.831	16.9	4.92
291 bars						
	42.2	3045	.147	.835	16.5	4.01
	76.8	3121	.147	.838	16.2	4.30
	69.6	3191	.146	.841	15.9	4.34
	153.6	3345	.145	.846	15.4	4.35
	360.0	3704	.143	.854	14.6	4.43
	669.6	4561	.140	.872	12.8	4.62
	1080	5641	.137	.888	11.2	4.71
	1080	6721	.135	.904	9.6	4.84
	1080	8881	.135	.914	8.6	5.6
	1080	9961	.135	.916	8.4	6.0
	1080	11041	.134	.917	8.3	6.34

S-17

G = 10-15

$h_o = 0.176$ $h_o - h_s = 0.175$ $r = 0.113$ $M = 0.2881$

σ and T	Δt	total t	h	D	%ϕ	$-(\text{Log } \dot{\varepsilon})$
176 bars 1173°						
	.2	.2	.174	.742	25.8	2.25
	2.4	3.0	.174	.744	25.6	2.84
	4.8	7.0	.173	.746	25.4	3.10
	9.6	17.0	.172	.749	25.1	3.34
	24.0	31.0	.171	.754	24.6	3.49
	24.0	55.0	.170	.759	24.1	3.67
	24.0	79.0	.169	.762	23.8	3.77
	12.0	91.0	.169	.765	23.5	3.85
	82.8	174.0	.178	.769	23.1	3.95
	120.0	294.0	.166	.778	22.3	4.03
	79.2	373.0	.165	.784	21.6	4.09
209 bars						
	54.5	434.0	.164	.790	21.0	3.94
	180.0	614.0	.162	.796	20.4	4.18
	134.4	748.0	.160	.804	19.6	4.26
176 bars						
	20.6	769.0	.160	.807	19.3	4.52
	20.9	790.0	.160	.808	19.2	4.53
243 bars						
	13.0	969.0	.160	.889	19.1	3.84
	127.2	1096.0	.159	.812	18.8	4.23
	180.0	1276.0	.158	.819	18.1	4.35

S-17, cont'd.

σ and T	Δt	total t	h	D	%φ	-(Log $\dot{\varepsilon}$)
243 bars (cont'd.)						
	180.0	1456.0	.156	.825	17.5	4.42
	6.0	1462.0	.156	.828	17.2	4.45
	312.0	1774.0	.155	.831	16.9	4.57
	9.6	1783.0	.155	.835	16.5	4.65
273 bars						
	39.5	1823.0	.155	.836	16.4	4.39
	42.0	1904.0	.154	.838	16.2	4.69
	201.6	2358.0	.153	.846	15.5	4.61
291 bars						
	22.6	2394.0	.153	.849	15.2	4.54
	82.8	2477.0	.152	.850	15.0	4.62
	10.8	2487.0	.152	.851	14.9	4.39
	799.2	3287.0	.150	.858	14.2	4.67
	1080.0	4367.0	.147	.874	12.6	4.72
	1080.0	5447.0	.144	.891	10.9	4.79
	1080.0	6527.0	.142	.905	9.49	4.89
	1080.0	7607.0	.140	.917	8.32	4.97
	1080.0	8687.0	.140	.923	7.7	5.85

S-18

G = 15-20

$h_o = 0.166$ $h_o - h_s = 0.166$ $r = 0.110$ $M = 0.2559$

σ and T	Δt	total t	h	D	%φ	$-(\text{Log } \dot{\varepsilon})$
169 bars, 1047°	1.2	1	.164	.744	25.6	2.47
	1.2	3	.164	.747	25.3	2.87
	1.2	4	.164	.748	25.2	2.99
	3.6	7	.164	.750	25.0	3.10
	4.8	12	.163	.752	24.9	3.42
	5.3	30	.163	.755	24.5	4.11
	112.8	142	.162	.757	24.3	4.34
	120.0	262	.161	.761	24.0	4.46
	120.0	382	.161	.763	23.7	4.68
	180.0	562	.160	.765	23.5	4.76
	180.0	742	.160	.767	23.3	4.82
	180.0	922	.159	.769	23.1	4.98
1112°	960.0	2362	.155	.784	21.6	4.56
1159°	360.0	2722	.152	.800	20.0	4.43
	360.0	3082	.151	.810	19.0	4.51
	360.0	3442	.149	.818	18.2	4.60
	360.0	3802	.148	.825	17.5	4.64

S-18, cont'd.

σ and T	Δt	total t	h	D	%ϕ	$-(\text{Log } \dot{\varepsilon})$
	741.6	4669	.146	.836	16.4	4.74
	871.2	5540	.144	.847	15.3	4.84
292 bars, 1159°						
	21.6	5663	.143	.857	14.3	4.67
	1065.6	6729	.402	.866	13.4	4.70
	1080.0	7809	.138	.882	11.8	4.83
	1080.0	8889	.136	.895	10.5	4.96
	1080.0	9969	.135	.905	9.5	4.99
	1080.0	11049	.134	.915	8.6	5.05
	1080.0	12129	.133	.922	7.8	5.16
	1080.0	13209	.132	.927	7.3	5.73

S-19

G = 25-53 (CO_2/CO)

$h_o = 0.176$ $h_o - h_s = 0.171$ $r = 0.124$ $M = 0.2806$

σ and T	Δt	total t	h	D	%φ	$-(\text{Log } \dot{\varepsilon})$
170 bars 1393°						
	1.9	2	.166	.624	37.6	1.76
	7.2	9	.163	.641	35.9	2.57
	12.0	21	.161	.652	34.8	2.99
	12.0	33	.160	.658	34.2	3.26
	12.0	45	.159	.662	33.8	3.38
	12.0	57	.158	.665	33.5	3.43
	14.4	72	.157	.668	33.2	3.51
	50.4	122	.155	.673	32.7	3.63
	96.0	218	.153	.683	31.7	3.73
	60.0	278	.151	.693	30.8	3.84
	60.0	338	.150	.698	30.2	3.97
	60.0	398	.150	.702	29.8	4.02
	60.0	458	.149	.706	29.4	4.07
	60.0	518	.148	.709	29.1	4.13
	60.0	578	.148	.712	28.8	4.19
	60.0	698	.146	.718	28.2	4.22
	55.2	802	.146	.722	27.8	4.27
	240.0	1042	.144	.727	27.3	4.36
	240.0	1282	.143	.734	26.7	4.46
	240.0	1522	.142	.739	26.1	4.52

S-19, cont'd.

σ and T	Δt	total t	h	D	%ϕ	$-(\mathrm{Log}\ \dot{\varepsilon})$
170 bars 1393° } cont'd.						
	240.0	1762	.141	.744	25.6	4.58
	432.0	2425	.139	.754	24.6	4.66
	180.0	2605	.139	.759	24.1	4.73
1548°						
	216.0	2821	.131	.781	21.9	3.58
	432.0	3253	.124	.825	17.5	3.92
	720.0	3973	.119	.865	13.5	4.24
	720.0	4693	.116	.895	10.5	4.46
	1080.0	5773	.113	.918	8.2	4.60
	1080.0	6853	.111	.941	6.0	4.72
	1080.0	7933	.109	.958	4.2	4.8
	1080.0	9013	.108	.971	2.9	4.97
	1080.0	10093	.107	.981	1.9	5.11
	1080.0	11173	.107	.086	1.4	5.64
	1080.0	12253	.106	.988	1.2	5.76

S-20

G = 25-53 (CO_2/CO)

$h_o = 0.179$ $h_o - h_s = 0.178$ $r = 0.124$ $M = 0.2927$

σ and T	Δt	total t	h	D	%ϕ	$-(\text{Log } \dot{\varepsilon})$
170 bars, 1413°						
	1.7	2	.173	.627	37.3	1.77
	4.8	7	.169	.644	35.6	2.28
	7.2	14	.166	.657	34.3	2.68
	12.0	26	.164	.667	33.3	2.93
	12.0	38	.162	.674	32.6	3.19
	12.0	50	.161	.679	32.1	3.30
	12.0	62	.160	.682	31.8	3.38
	12.0	86	.159	.688	31.2	3.56
	12.0	110	.158	.692	30.8	3.58
	33.6	155	.157	.697	30.3	3.79
	60.0	215	.156	.701	29.9	3.88
	60.0	275	.155	.706	29.4	3.97
	60.0	335	.154	.711	28.9	4.00
	60.0	395	.153	.715	28.5	4.03
	60.0	455	.152	.719	28.1	4.08
	60.0	695	.150	.730	27.0	4.20
	60.5	815	.149	.736	26.5	4.25

S-20, cont'd.

σ and T	Δt	total t	h	D	%ϕ	-(Log $\dot{\varepsilon}$)
246 bars						
1413°						
	10.1	842	.148	.741	25.9	3.51
	63.6	910	.147	.745	25.5	3.87
	60.0	970	.146	.751	24.9	3.97
	60.0	1030	.145	.755	24.5	4.06
	60.0	1090	.144	.759	24.1	4.07
	60.0	1210	.143	.766	23.4	4.21
	60.0	1330	.142	.772	22.8	4.26
	48.0	1558	.140	.782	21.8	4.31
	120.0	1764	.139	.787	21.3	4.38
	120.0	2004	.138	.795	20.5	4.44
	120.0	2124	.137	.798	20.2	4.47
	120.0	2484	.136	.809	19.1	4.51
	100.8	2585	.135	.811	18.9	4.57
	223.2	2995	.134	.816	18.4	4.73
246 bars						
1541°						
	158.4	3154	.132	.825	17.5	3.96
1545°						
	187.2	3341	.128	.845	15.5	3.79
	432.0	3773	.123	.876	12.4	4.00
	648.0	4421	.118	.912	8.8	4.26
	360.0	4781	.117	.935	6.5	4.43
	720.0	5501	.114	.952	4.9	4.51

S-20, cont'd.

σ and T	Δt	total t	h	D	%ϕ	$-(\text{Log } \dot{\varepsilon})$
246 bars						
1545°						
	720.0	6221	.113	.968	3.2	4.74
	720.0	6941	.112	.989	2.0	4.85
	720.0	7661	.111	.987	1.3	5.18
	720.0	9821	.110	.997	0.4	5.60

REFERENCES

Aitkin, R. B. and R. M. Fulrath, Point Defects and the Sintering of Lead Zirconate-Titanate, J. Amer. Ceram. Soc., 54, 5, 265-270, 1971.

Aitkins, E. A., Initial Sintering Kinetics of Beryllium Oxide, J. Amer. Ceram. Soc., 43, 627-633, 1960.

Ashby, M. F., A First Report on Deformation Mechanism Maps, Acta. Met., 20, 887, 1972.

Ashby, M. F., A First Report on Sintering Diagrams, Acta. Met., 22, 275-289, 1974.

Ashby, M. F. and R. A. Verrall, Diffusion-Accommodated Flow in Superplasticity, Acta. Met., 21, 149-163, 1973.

Astbury, N. F., Deformation and Fracture, Brit. Ceram. Soc. Trans., 68, 1, 1-7, 1969.

Barmore, W. L. and R. R. Vandervoort, High-Temperature Creep and Dislocation Etch Pits in Polycrystalline Beryllium Oxide, J. Amer. Ceram. Soc., 50, 316-320, 1967.

Barmore, W. L. and R. R. Vandervoort, High-Temperature Plastic Deformation of Polycrystalline Beryllium Oxide, J. Amer. Ceram. Soc., 48, 499-505, 1965.

Bell, H. and V. Krishnamachari, and J. T. Jones, Compressive Creep of Rutile at High Temperatures, J. Amer. Ceram. Soc., 54, 7, 359-360, 1971.

Bentle, G. G. and R. M. Kniefel, Brittle and Plastic Behavior of Hot Pressed BeO, J. Amer. Ceram. Soc., 40, 570-577, 1965.

Boullier, A. M. and Y. Gueguen, SP-Mylonites: Origin of Some Mylonite by Superplastic Flow, Contrib. Mineral. Petrol., 50, 93-104, 1975.

Brace, W. F. and J. B. Walsh, Some Direct Measurements of the Surface Energy of Quartz and Orthoclase, The Amer. Mineral., 47, 1111-1122, 1962.

Budworth, D. W., Theory of Pore Closure During Sintering, Brit. Ceram. Soc. Trans., 69, 29-31, 1970.

Canon, R. F. and J. T. A. Roberts and R. J. Beals, Deformation of UO_2 at High Temperature, J. Amer. Ceram. Soc., 54, 2, 105-112, 1971.

Cannon, W. R. and O. D. Sherby, Third-Power Stress Dependence in Creep of Polycrystalline Nonmetals, J. Amer. Ceram. Soc., 56, 3, 157-161, 1973.

Carter, N. L. and H. G. Ave'Lallemant, High Temperature Flow of Dunite and Peridotite, Geol. Soc. Amer. Bull., 81, 2181-2202, 1970.

Chang, R., Creep of Al_2O_3 Single Crystals, J. Appl. Phys., 31, 484-487, 1960.

Coble, R. L., A Model for Boundary Diffusion Controlled Creep in Polycrystalline Materials, J. Appl. Phys., 34, 6, 1679-1682, 1963.

Coble, R. L., Diffusional Models for Hot-Pressing with Surface Energy and Pressure Effects as Driving Forces, J. Appl. Phys., 41, 12, 4798-4807, 1970.

Coble, R. L., Sintering Alumnia: Effect of Atmosphere, J. Amer. Ceram. Soc., 45, 3, 123-126, 1962.

Crouch, A. G., High Temperature Deformation of Polycrystalline Fe_2O_3, J. Amer. Ceram. Soc., 55, 11, 559-563, 1972.

Dutta, S. K. and G. E. Gazza, Properties of Hot-Pressed SiB_6, Amer. Ceram. Soc. Bull., 52, 552-554, 1973.

Durham, W. B., Plastic Flow of Single-Crystal Olivine, Ph.D. Thesis, M.I.T., Cambridge, Mass., 1975.

Eshelby, J. D., The Determination of the Elastic Field of an Ellipsoidal Inclusion, and Related Problems, Proc. Roy. Soc., A241, 376-396.

Farnsworth, P. L. and R. L. Coble, Deformation Behavior of Dense Polycrystalline SiC, J. Amer. Ceram. Soc., 49, 264-268, 1966.

Felten, E. J., Hot-Pressing of Alumina Powders at Low Temperatures, J. Amer. Ceram. Soc., 44, 381-385, 1961.

Fryer, G. M., Pressure-Sintering of Alumina, Brit. Ceram. Soc. Trans., 68, 5, 185-189, 1969.

Gifkins, R. C., Diffusional Creep Mechanisms, J. Amer. Ceram. Soc., 51, 69-72, 1968.

Gifkins, R. C., Superplasticity During Creep, J. Inst. Metals, 95, 373-376, 1967.

Goetze, C. and D. L. Kohlstedt, Laboratory Study of Dislocation Climb and Diffusion in Olivine, J. Geophys. Res., 78, 5961-5971, 1973.

Grant, N. J. and A. W. Mullendore, ed., Deformation and Fracture at Elevated Temperatures, The M.I.T. Press, Cambridge, Mass., 1965.

Hayden, H. W. and S. Floreen and P. D. Goodell, The Deformation Mechanisms of Superplasticity, Metall. Trans., 3, 833-842, 1972.

Herring, C., Diffusional Viscosity of a Polycrystalline Solid, J. Appl. Phys., 21, 437-445, 1950.

Hirthe, W. M. and J. O. Brittain, High Temperature Steady-State Creep in Rutile, J. Amer. Ceram. Soc., 46, 411-417, 1963.

Jaeger, J. C., Elasticity, Fracture and Flow, Methuen and Co., Ltd., London, 1956.

Johnson, R. H., Superplasticity, Metall. Rev., 15, 115-134, 1970.

Kingery, W. D., Introduction to Ceramics, John Wiley and Sons, Inc., New York, p. 44, 1960.

Kirby, Stephen H. and C. B. Raleigh, Mechanisms of High-Temperature Solid-State Flow in Minerals and Ceramics and Their Bearing on the Creep Behavior of the Mantle, Tectonophysics, 19, 165-194, 1973.

Klingsberg, C., ed., The Physics and Chemistry of Ceramics, Gordon and Breach Science Publishers, New York, 1963.

Kohlstedt, D. L. and C. Goetze, Low-Stress High-Temperature Creep in Olivine Single Crystals, J. Geophys. Res., 79, 14, 2045-2051, 1974.

Lambe, T. W. and R. V. Whitman, Soil Mechanics, John Wiley and Sons, Inc., New York, 1969.

Langdon, T. G. and J. A. Pask, The Mechanism of Creep in Polycrystalline Magnesium Oxide, Acta. Metall., 18, 505-510, 1970.

McClelland, J. D., A Plastic Flow Model of Hot-Pressing, J. Amer. Ceram. Soc., 44, 526 , 1961.

McClintock, F. A. and A. S. Argon, ed., Mechanical Behavior of Materials, Addison-Wesley, Reading, Mass., 1966.

Muan, A. and E. F. Osborne, Phase Equilibria Among Oxides in Steelmaking, Addison-Wesley, Reading, Mass., p. 26 and 50, 1965.

Mukherjee, A. K., The Rate Controlling Mechanism in Superplasticity, Mater. Sci. Eng., 8, 83-89, 1971.

Murray, P. and D. T. Livey and J. Williams, The Hot-Pressing of Ceramics, in Ceramics Fabrication Processes, W. D. Kingery (ed.), M.I.T. Press, 147-170, 1958.

Nabarro, F. R. N., Steady-State Diffusional Creep, Phil. Mag., 16, 231-237, 1967.

Nitzen, V. Stability Field of Olivine with Respect to Oxidation and Reduction, J. Geophys. Res., 79, 706-711, 1974.

Nohs, M. R. Interpretation of Kinetics of Final-Stage Pressure-Sintering of NiO by Deformation Mechanism Maps, J. Amer. Ceram. Soc., 57, 6, 271, 1974.

Poteat, L. E. and C. S. Yust, Creep of Polycrystalline Thorium Dioxide, J. Amer. Ceram. Soc., 49, 410-414, 1966.

Radford, K. C. and G. R. Terwilliger, High Temperature Deformation of Ceramics: II, Specific Behavior, Ceram. Bull., 53, 6, 465-472, 1974.

Raleigh, C. B., Glide Mechanisms in Experimentally Deformed Minerals, Science, 150, 739-741, 1965.

Raleigh, C. B., Mechanisms of Plastic Deformation of Olivine, J. Geophys. Res., 73, 5391-5406, 1968.

Raleigh, C. B., Plastic Deformation of Upper Mantle Silicate Minerals, Geophys. J. Roy. Astron. Soc., 14, 45-56, 1967.

Raleigh, C. B. and S. H. Kirby, Creep in the Upper Mantle, Mineral. Soc. Amer. Spec. Pap. 3, 113-121, 1970.

Ramakrishnan, P., Hot-Pressing of MgO, Brit. Ceram. Soc. Trans., 67, 135-145, 1968.

Rao, A. S. and A. C. D. Chaklader, Plastic Flow During Hot-Pressing, J. Amer. Ceram. Soc., 55, 12, 596-601, 1972.

Rossi, R. C. and R. M. Fulrath, Final Stage Densification in Vacuum Hot-Pressing of Alumina, J. Amer. Ceram. Soc., 48, 558-564, 1965.

Shelley, D., Manual of Optical Mineralogy, Elsevier Scientific Publ. Co., Amsterdam, 1975.

Sherby, O. D. and P. M. Burke, Mechanical Behavior of Crystalline Solids at Elevated Temperatures, Prog. Mater. Sci., 13, 325-429, 1968.

Shewmon, P. G., Diffusion in Solids, McGraw-Hill Book Co., New York, 1963.

Simmons, G. and H. Wang, Single Crystal Elastic Constants and Calculated Aggregate Properties: A Handbook, The M.I.T. Press, Cambridge, Mass., 1971.

Stellrecht, D. E. and M. S. Farkas, and D. P. Moak, Compressive Creep of Uranium Carbide, J. Amer. Ceram. Soc., 51, 455-458, 1968.

Stocker, R. L. and M. F. Ashby, On the Rheology of the Upper Mantle, Rev. Geophys. Space Phys., 11, 2, 391-426, 1973.

Terwilliger, G. T. and F. F. Lange, Hot-Pressing Behavior of Si_3N_4, J. Amer. Ceram. Soc., 57, 1, 1974.

Terwilliger, G. R. and K. C. Radford, High Temperature Deformation of Ceramics: I, Background, Ceram. Bull., 53, 172-179, 1974.

Tickell, F. G., The Techniques of Sedimentary Mineralogy, Elsevier Publ. Co., Amsterdam, 1965.

Vandervoort, R. R. and Barmore, W. L., Compressive Creep of Polycrystalline BeO, J. Amer. Ceram. Soc., 48, 180-184, 1963.

Warshaw, S. I. and F. H. Norton, Deformation Behavior of Polycrystalline Aluminum Oxide, J. Amer. Ceram. Soc., 45, 10, 479-487, 1962.

Weertman, J., The Creep Strength of the Earth's Mantle, Rev. Geophys. Space Phys., 8, 1, 145-168, 1970.

Weertman, J., Dislocation Climb Theory of Steady-State Creep, Trans. ASM, 61, 681-694, 1968.

Weertman, J. and J. R. Weertman, High Temperature Creep of Rock and Mantle Viscosity, Ann. Rev. Earth Planet. Sci., 3, 243-315, 1975.

Wilkinson, D. S. and M. F. Ashby, Pressure Sintering by Power Law Creep, preprint, 1975.

Wilkinson, D. S. and M. F. Ashby, The Development of Pressure Sintering Maps, to be published in The Proceedings of the Fourth International Conference on Sintering and Related Phenomena, May 26-28, 1975.

ADDITIONAL REFERENCES

Ahrens, T. J. amd D. L. Anderson and A. E. Ringwood, Equation of State and Crystal Structures of High-Pressure Phases of Shocked Silicates and Oxides, *Rev. Geophys.*, *7*, 667-709, 1969.

Anderson, D. L. and H. Kanamori, Shock-Wave Equations of State For Rocks and Minerals, *J. Geophys, Res.*, *73*, 6477-6503, 1968.

Bradley, R. S. and A. K. Jamil and D. C. Munro, The Electrical Conductivity of Olivine at High Temperatures and Pressures, *Geochim. Cosmochim. Acta*, *28*, 11, 1669-1678, 1964.

Caristan, Y., private communication, 1976.

Duba, A., Electrical Conductivity of Olivine, *J. Geophys, Res.*, *77*, 2483-2495, 1972.

Dvořák, Z., Electrical Conductivity of Several Samples of Olivines, Peridotities, and Dunites As a Function of Pressure and Temperature, *Geophys.*, *38*, 1, 14-24, 1973.

Nicholas, A. and F. Boudier and A. M. Bollier, Mechanisms of Flow In Naturally and Experimentally Deformed Peridotites, *Am. J. Sci.*, *273*, 853-876, 1973.

Passmore, E. M. and R. H. Duff and T. Vasilos, Creep of Dense, Polycrystalline Magnesium Oxide, *J. Amer. Cer. Soc.*, *49*, 11, 594-600, 1966.

Paterson, M. S. and C. W. Weaver, Deformation of Polycrystalline MgO Under Pressure, *J. Amer. Ceram. Soc.*, *53*, 463-471, 1970.

Twiss, R. D., Structural Superplastic Creep and Linear Viscoscity in the Earth's Mantle, *Earth and Planet. Sci. Let.*, (in press), 1976.

Underwood, E. E. Quantitative Stereology for Microstructural Analysis, in *Microstructural Analysis: Tools and Techniques*, McCall, J. L. and W. M. Mueller (ed.), Plenum Press, New York, pp. 42-43, 1973.